

Wavelet-Based Density Estimation for Persistent Homology

Konstantin Häberle^{1,2,†}, Barbara Bravi^{1,†}, and Anthea Monod^{1,†}

1 Department of Mathematics, Imperial College London, UK

2 Chair for Mathematical Information Science, ETH Zurich, Switzerland

† Corresponding e-mails: haeberlk@ethz.ch; b.bravi21@imperial.ac.uk; a.monod@imperial.ac.uk

Abstract

Persistent homology is a central methodology in topological data analysis that has been successfully implemented in many fields and is becoming increasingly popular and relevant. The output of persistent homology is a persistence diagram—a multiset of points supported on the upper half plane—that is often used as a statistical summary of the topological features of data. In this paper, we study the random nature of persistent homology and estimate the density of expected persistence diagrams from observations using wavelets; we show that our wavelet-based estimator is optimal. Furthermore, we propose an estimator that offers a sparse representation of the expected persistence diagram that achieves near-optimality. We demonstrate the utility of our contributions in a machine learning task in the context of dynamical systems.

Keywords: Nonparametric density estimation; wavelets; persistent homology; persistence measures.

1 Introduction

Topological data analysis (TDA) is a recent field of data science emanated from applied and computational topology that extracts and studies topological information from complex and high-dimensional data structures using theory from algebraic topology. A fundamental method in TDA is *persistent homology*, which adapts the classical algebraic topological concept of *homology* to study topological invariants associated with a dataset; while the homology of a dataset corresponds to its “shape,” persistent homology captures both the “shape” and “size” of the dataset. Persistent homology has been successfully employed in a variety of applications including signal analysis (Perea & Harer, 2015), computer vision (Li *et al.*, 2014), cancer patient survival (Crawford *et al.*, 2020), and viral evolution (Monod *et al.*, 2019), and is becoming an increasingly popular technique in data analysis.

Persistence diagrams are the resulting objects of persistent homology; they encode the lifetimes of topological features of datasets and thus exhibit a random nature. The randomness of persistence diagrams is a challenging topic of study because the algebraic construction of persistent homology induces a highly complex geometric space (Turner *et al.*, 2014). In this paper, we focus on persistence diagrams in random settings and study their distributional behavior nonparametrically using methods from uncertainty quantification. Specifically, we propose a Haar wavelet estimator to estimate the *expected persistence diagram*, which, under mild assumptions, is known to be absolutely continuous with respect to the Lebesgue measure and therefore has a Lebesgue density (Chazal & Divol, 2019). We prove that the Haar wavelet estimator is *minimax*: its maximal risk is minimal among all possible estimators of the expected persistence diagram. Furthermore, we also propose a thresholding Haar wavelet estimator, which offers a sparse (or *compressed*) representation of the expected persistence diagram and thus computational advantages in practical settings, and show that it achieves near-optimal minimax rates. This paper is, to the best of our knowledge, the first to use wavelet estimators to estimate expected persistence diagrams.

Our work is largely inspired by previous work by Chazal & Divol (2019), who propose a kernel density estimator (KDE) and prove its convergence to the true density function in the L^2 -norm. However, it has since been shown by Divol & Lacombe (2021a) that the *optimal partial transport* metric OT_p , rather than the L^2 metric, is the natural metric for expected persistence diagrams; this metric was used to show that the empirical mean of persistence diagrams is minimax. The resulting proposed estimator, however, does not have a Lebesgue density in general and its support moreover tends to be very large, making it impractical in

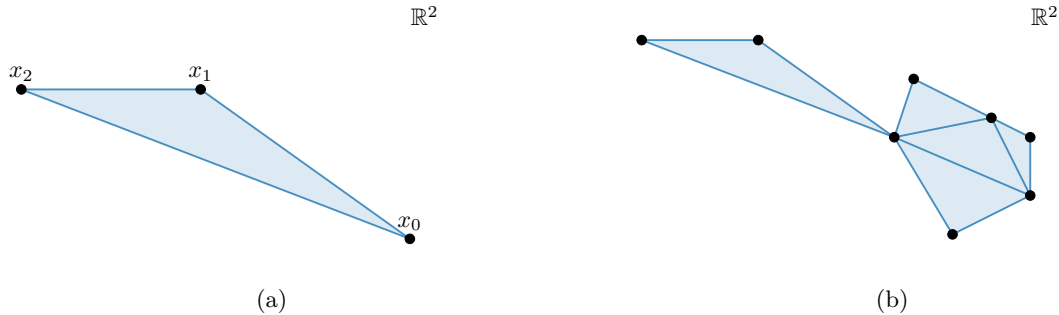


Figure 1: (a) 2-simplex formed by 3 affinely independent points $x_0, x_1, x_2 \in \mathbb{R}^2$. (b) Simplicial complex consisting of 2-simplices.

applications. In addition to our proposed Haar wavelet comprising a Lebesgue density and our thresholding Haar wavelet being sparse, compared to KDEs, Haar wavelets have the advantage of being locally adaptive. The local adaptivity property enables a finer local analysis, which may be more difficult to achieve with kernels depending on choice of bandwidth.

The remainder of this paper is organized as follows. Section 2 provides the formal background to persistent homology, persistence measures, and their resulting metric space, which is the context of our work. Section 3 presents our main result of minimaxity of wavelet estimators for expected persistence diagrams as well as the thresholding wavelet estimators and discusses their properties. Section 4 presents numerical experiments and verifications of our derived theory. Furthermore, we provide a practical implementation of our work to a classification problem in the context of dynamical systems. We conclude our paper with a discussion of our work and some ideas for future research in Section 5.

2 Preliminaries

In this section, we overview the construction of persistence diagrams from persistent homology and discuss their properties. We then present the generalization of persistence diagrams to persistence measures as the setting in which we work. In particular, we present the expected persistence diagram as our object of study which we aim to estimate.

In addition, we recall basic concepts and results from wavelet theory that are essential for constructing nonparametric density estimators.

2.1 Persistent Homology

Persistent homology studies the topological features of a simplicial complex or topological space across multiple scales. In particular, it tracks the evolution of connected components, loops, and higher-dimensional cavities with respect to a nested sequence of topological spaces, i.e., a *filtration*. For computational feasibility due to the existence of efficient algorithms, discretizations of these topological spaces are often considered in the form of simplices and simplicial complexes that can be seen as skeletal representations of the topological space. A k -simplex is the convex hull of $k + 1$ affinely independent points x_0, x_1, \dots, x_k ; a set of k -simplices assembled in a combinatorial fashion forms a simplicial complex K . See Figure 1 for an illustration.

Given a point cloud X , an important and widely-used simplicial complex is the *Vietoris-Rips (VR) complex*, used to build the Vietoris-Rips (or simply Rips) filtration $(K_t)_{t \geq 0} := (\text{VR}(X, t))_{t \geq 0}$. The VR complex for X and filtration parameter t , denoted $\text{VR}(X, t)$, is the simplicial complex whose vertex set is X , where $\{x_0, \dots, x_k\} \subseteq X$ spans a k -simplex if and only if the diameter between two points, x_i and x_j , is less than the threshold value, t : $d^X(x_i, x_j) \leq t$, for all $i, j \in \{0, 1, \dots, k\}$, where d^X denotes a metric on X . In this paper, we focus on point clouds as our topological space of interest and their discretization by VR complexes.

Computing the k th simplicial homology groups $H_k(K_t)$ with coefficients in a field for dynamic values of $t \geq 0$ yields a sequence of vector spaces. Note that $K_t \subseteq K_{t'}$ whenever $t \leq t'$, which induces linear

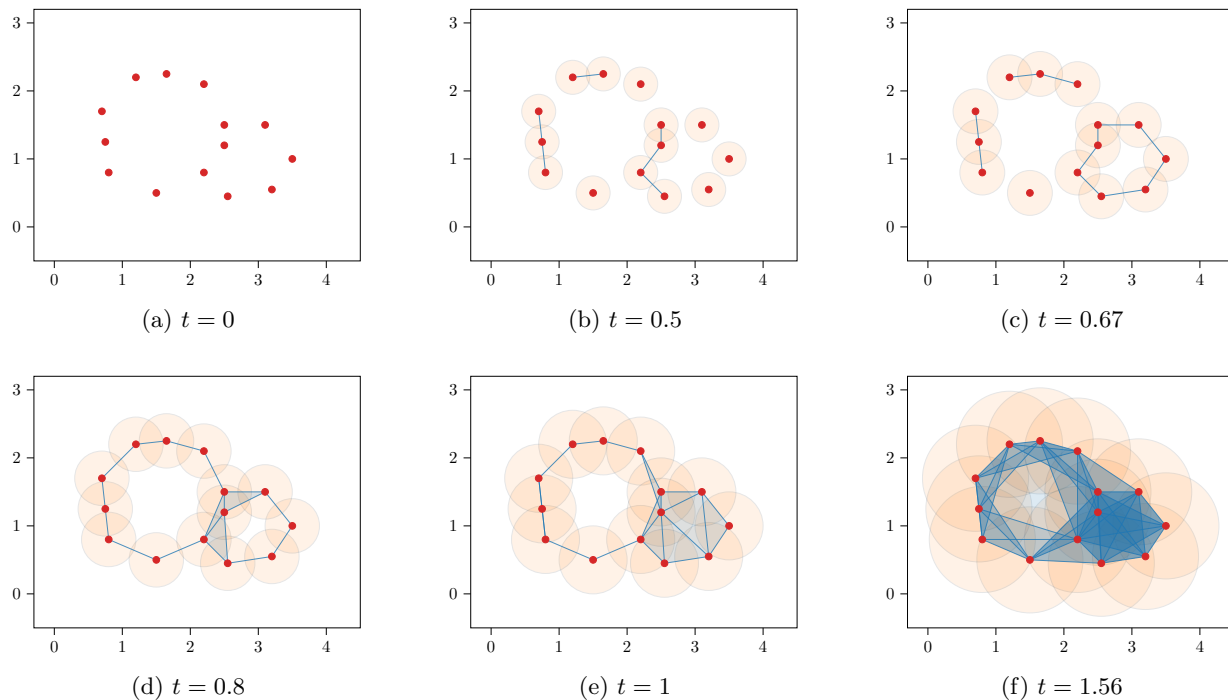


Figure 2: Constructing a simplicial complex from a point cloud using the Vietoris–Rips complex. (a) The initial point cloud X is obtained for $t = 0$ corresponding to the birth of all 0-dimensional features (connected components). (b) Some connected components have died due to the creation of 1-simplices. (c) A 1-dimensional hole (loop) has appeared. (d) The second loop has been created while all but one of the connected components have vanished. (e) The first loop has been filled yielding its death. (f) All loops have disappeared; only the connected component of infinite persistence remains.

maps between $H_k(K_t)$ and $H_k(K_{t'})$. The family of vector spaces together with their linear maps is called a *persistence module*. Persistence modules are uniquely decomposable into a direct sum of interval modules up to permutations (Zomorodian & Carlsson, 2005). The collection of these indecomposables is referred to as a *barcode* where the intervals are *bars*, each representing the evolution of a topological feature (k -dimensional hole). In particular, if $(t_1, t_2) \subset \mathbb{R}$ is such an interval, then the corresponding topological feature appears at scale t_1 in the filtration $(K_t)_{t \geq 0}$ and disappears at scale t_2 . We call t_1 and t_2 the *birth* and *death times*, respectively. This information can be encoded in a *persistence diagram* by taking birth and death times as ordered pairs and plotting them. The persistence diagram is then the output of persistent homology, see Figures 2 and 3.

Definition 1 (Persistence diagram). A *persistence diagram* is a locally finite multiset of points supported on $\Omega := \{(t_1, t_2) \in \mathbb{R}^2 : t_1 < t_2\}$ together with points on the diagonal $\partial\Omega := \{(t, t) \in \mathbb{R}^2\}$ counted with infinite multiplicity.

Distances Between Persistence Diagrams. The collection of all persistence diagrams constitutes a metric space when equipped with an appropriate distance function. There exist various metrics on the space of persistence diagrams; we focus on the following two distance functions that are widely used in computations and applications in TDA.

Definition 2. Let D and D' be two persistence diagrams, and let $1 \leq q \leq \infty$. For $1 \leq p < \infty$, the p -Wasserstein distance between D and D' is given by

$$W_{p,q}(D, D') := \inf_{\gamma} \left(\sum_{x \in D \cup \partial\Omega} \|x - \gamma(x)\|_q^p \right)^{1/p}, \quad (1)$$

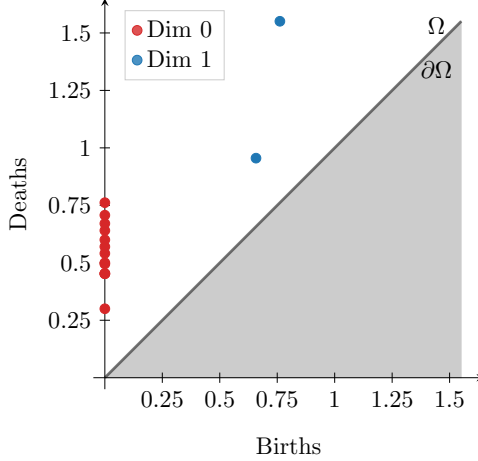


Figure 3: Persistence diagram obtained from the Vietoris–Rips filtration of the point cloud X shown in Figure 2 illustrating the birth and death times of the 0- and 1-dimensional holes. Here, the 0-dimensional feature of infinite persistence is discarded.

where the infimum is taken over all bijections γ between $D \cup \partial\Omega$ and $D' \cup \partial\Omega$. For $p = \infty$, the *bottleneck distance* is given by

$$W_{\infty,q}(D, D') := \inf_{\gamma} \sup_{x \in D \cup \partial\Omega} \|x - \gamma(x)\|_q. \quad (2)$$

Whenever $p = q$, we write $W_p(\cdot, \cdot) := W_{p,p}(\cdot, \cdot)$ for notational simplicity. A bijection γ that achieves (1) (or (2)) is called an *optimal matching*. The p -total persistence of a persistence diagram D is given by

$$\text{Pers}_p(D) := \left(\sum_{x \in D} \|x - x^\perp\|_q^p \right)^{1/p}, \quad 1 \leq p < \infty,$$

where x^\perp denotes the orthogonal projection of x onto $\partial\Omega$. For $p = \infty$, set

$$\text{Pers}_\infty(D) := \sup_{x \in D} \|x - x^\perp\|_q.$$

Denote by \mathcal{D}^p the set of persistence diagrams D with finite p -total persistence, $\text{Pers}_p(D) < \infty$.

The space of persistence diagrams, as random objects, is a setting where probabilistic and statistical studies are valid: the metric space $(\mathcal{D}^p, W_{p,q})$ is complete and separable for any $1 \leq p < \infty$ and $1 \leq q \leq \infty$ (Mileyko *et al.*, 2011). As a result, probability measures on $(\mathcal{D}^p, W_{p,q})$ are well-defined, which implies the existence of other standard statistical and probabilistic objects on $(\mathcal{D}^p, W_{p,q})$ such as expectations and variances. However, geometrically, the metric space of persistence diagrams when $p = 2$ is highly nonlinear (and as yet geometrically uncharacterized for $p > 2$), which makes even simple statistical and machine learning tasks with persistence diagrams very challenging (Turner *et al.*, 2014). To deal with this issue, persistence diagrams are typically embedded into a Banach or Hilbert space via vectorizations, such as explicit feature maps (Bubenik, 2015; Adams *et al.*, 2017) or implicit kernel methods (Reininghaus *et al.*, 2015). Note, however, that the metric structure of the space of persistence diagrams is not preserved by these embeddings (Bubenik & Wagner, 2020).

Persistence Measures. Persistence diagrams generalize well to a measure-theoretic setting, which has desirable probabilistic and statistical properties (Chazal & Divol, 2019). Since persistence diagrams are simply multisets of points supported on Ω , it is natural to represent a persistence diagram as a discrete measure in the following manner. Let $D \in \mathcal{D}^p$, then

$$D = \sum_x \delta_x, \quad (3)$$

where δ_x denotes the Dirac measure in $x \in \Omega$, and where the sum is taken over all points $x = (t_1, t_2)$ that belong to the persistence diagram D . Points in D corresponding to topological features of infinite persistence are disregarded in the representation (3).

Typically, the underlying point cloud X of a persistence diagram D is random so that D becomes a random measure. To analyze the expected behavior of any linear descriptor of the form $\Psi_h(D) := \int_{\Omega} h \, dD$, for some Banach space-valued function h on Ω , it suffices to study the *expected persistence diagram*.

Definition 3 (Expected persistence diagram, (Chazal & Divol, 2019)). Let D be a persistence diagram resulting from a random point cloud. The *expected persistence diagram (EPD)* is defined to be the deterministic measure

$$\mathbb{E}[D](A) := \mathbb{E}[D(A)], \quad \text{for all Borel sets } A \subset \Omega.$$

Chazal & Divol (2019) show that the expected persistence diagram has a density with respect to the Lebesgue measure. The expected persistence diagram is in general not a persistence diagram, but lies in a natural extension of the space of persistence diagrams, namely, the space of *persistence measures* (Divol & Lacombe, 2021b). The space of persistence measures \mathcal{M}^p , $1 \leq p \leq \infty$, is defined to be the set of all non-negative Radon measures μ supported on Ω such that $\text{Pers}_p(\mu) < \infty$. Here,

$$\text{Pers}_p(\mu) := \begin{cases} \int_{\Omega} \|x - x^{\perp}\|_q^p \, d\mu(x) & \text{if } 1 \leq p < \infty, \\ \sup_{x \in \text{supp}(\mu)} \|x - x^{\perp}\|_q & \text{if } p = \infty, \end{cases} \quad \text{for } 1 \leq q \leq \infty.$$

Equip the space of persistence measures \mathcal{M}^p with the following metric (Divol & Lacombe, 2021b): for $\mu, \nu \in \mathcal{M}^p$, define

$$\text{OT}_{p,q}(\mu, \nu) := \inf_{\gamma \in \text{Adm}(\mu, \nu)} \left(\int_{\bar{\Omega} \times \bar{\Omega}} \|x - y\|_q^p \, d\gamma(x, y) \right)^{1/p}, \quad 1 \leq p < \infty, \quad (4)$$

where $\bar{\Omega} := \Omega \cup \partial\Omega$, and where $\text{Adm}(\mu, \nu)$ denotes the set of Radon measures γ on $\bar{\Omega} \times \bar{\Omega}$ such that

$$\gamma(A \times \bar{\Omega}) = \mu(A) \text{ and } \gamma(\bar{\Omega} \times B) = \nu(B), \text{ for all Borel sets } A, B \subset \Omega.$$

For $p = \infty$,

$$\text{OT}_{\infty,q}(\mu, \nu) := \inf_{\gamma \in \text{Adm}(\mu, \nu)} \sup_{(x,y) \in \text{supp}(\gamma)} \|x - y\|_q.$$

Whenever $p = q$, we will use the simplified notation $\text{OT}_p(\cdot, \cdot) := \text{OT}_{p,p}(\cdot, \cdot)$. We now recall the following results established by Divol & Lacombe (2021b): The space $(\mathcal{M}^p, \text{OT}_{p,q})$ is complete and separable for $1 \leq p < \infty$ and $1 \leq q \leq \infty$. The space $(\mathcal{M}^{\infty}, \text{OT}_{\infty,q})$ is complete but not separable for any $1 \leq q \leq \infty$. Note that \mathcal{D}^p is closed in \mathcal{M}^p with respect to $\text{OT}_{p,q}$. Moreover, for any $\mu, \nu \in \mathcal{D}^p$, it holds that

$$W_{p,q}(\mu, \nu) = \text{OT}_{p,q}(\mu, \nu).$$

Thus, $(\mathcal{M}^p, \text{OT}_{p,q})$ is a natural and proper extension of the space of persistence diagrams $(\mathcal{D}^p, W_{p,q})$. Due to its linear structure the space of persistence measures \mathcal{M}^p is very convenient for both computation and statistical analyses.

2.2 Wavelets

Switching perspectives, we now recall some basic elements of wavelet theory.

A wavelet expansion of a function $f \in L^2(\mathbb{R}^2)$ corresponds to a multiscale decomposition of f , which is obtained by writing f as a sum of its coarse approximation and its local fluctuations. More precisely, consider the closed linear subspace $\overline{\text{span}(\mathcal{V}_j)}$ of $L^2(\mathbb{R}^2)$, which is generated by some function $\varphi : \mathbb{R}^2 \rightarrow \mathbb{R}$ according to

$$\mathcal{V}_j := \{2^j \varphi(2^j \cdot + \ell) : \ell \in \mathbb{Z}^2\}, \quad j \in \mathbb{Z}.$$

For an appropriate choice of φ , there exists a nested sequence of closed linear subspaces

$$\cdots \subset \overline{\text{span}(\mathcal{V}_{-1})} \subset \overline{\text{span}(\mathcal{V}_0)} \subset \overline{\text{span}(\mathcal{V}_1)} \subset \cdots \quad (5)$$

such that

- (i) $\bigcap_{j \in \mathbb{Z}} \overline{\text{span}(\mathcal{V}_j)} = \{0\}$,
- (ii) $\bigcup_{j \in \mathbb{Z}} \overline{\text{span}(\mathcal{V}_j)}$ is dense in $L^2(\mathbb{R}^2)$,
- (iii) \mathcal{V}_0 is an orthonormal basis of $\overline{\text{span}(\mathcal{V}_0)}$, and
- (iv) for all $h \in L^2(\mathbb{R}^2)$ and all $j \in \mathbb{Z}$, $h \in \overline{\text{span}(\mathcal{V}_j)} \iff h(2 \cdot) \in \overline{\text{span}(\mathcal{V}_{j+1})}$.

If these conditions are satisfied, $\{\overline{\text{span}(\mathcal{V}_j)}\}_{j \in \mathbb{Z}}$ is called a *multiresolution approximation* of $L^2(\mathbb{R}^2)$ and φ its *scaling function* (Cohen, 2003). Thus, projecting $f \in L^2(\mathbb{R}^2)$ onto the subspace $\overline{\text{span}(\mathcal{V}_j)}$ gives a coarse approximation of f if j is small and a fine approximation if j is large. The details (fluctuations) complementing the approximation between $\overline{\text{span}(\mathcal{V}_j)}$ and $\overline{\text{span}(\mathcal{V}_{j+1})}$ may be governed by the set

$$\mathcal{W}_j := \{2^j \psi^a(2^j \cdot + \ell), 2^j \psi^b(2^j \cdot + \ell), 2^j \psi^c(2^j \cdot + \ell) : \ell \in \mathbb{Z}^2\}$$

for some functions $\psi^a, \psi^b, \psi^c: \mathbb{R}^2 \rightarrow \mathbb{R}$ according to

$$\overline{\text{span}(\mathcal{V}_{j+1})} = \overline{\text{span}(\mathcal{V}_j)} \oplus \overline{\text{span}(\mathcal{W}_j)}. \quad (6)$$

Applying (6) recursively, using (5), and the fact that $\bigcup_{j \in \mathbb{Z}} \overline{\text{span}(\mathcal{V}_j)}$ is dense in $L^2(\mathbb{R}^2)$,

$$L^2(\mathbb{R}^2) = \overline{\text{span}(\mathcal{V}_{j_0})} \oplus \bigoplus_{j \geq j_0} \overline{\text{span}(\mathcal{W}_j)},$$

for every $j_0 \in \mathbb{N}_0$. Thus, the wavelet expansion of $f \in L^2(\mathbb{R}^2)$ reads

$$f = \sum_{\phi \in \mathcal{V}_{j_0}} \alpha_\phi \phi + \sum_{j \geq j_0} \sum_{\psi \in \mathcal{W}_j} \beta_\psi \psi,$$

where $\alpha_\phi, \beta_\psi \in \mathbb{R}$ are the wavelet coefficients of this expansion. This decomposition allows for a multiresolution representation of the approximated function because it is equivalent to a description at different scales, where at each scale there exists both a coarse- and fine-grained approximation of the function. Indeed, the first term is a (coarse) approximation of f at scale j_0 ; the second term describes the fine details (fluctuations) (Cohen, 2003; Härdle *et al.*, 2012).

Approximation with Wavelets. Wavelet transforms are a popular choice for modeling signals and images and for nonparametric density estimation (Abramovich *et al.*, 2000; Härdle *et al.*, 2012), thanks to their ability to approximate large classes of functions and to provide a locally accurate representation of the data structure. Wavelets are well known to achieve considerable approximation power in connection to a broad class of functions. Their localized structure (both in space and frequency) allows them to behave smoothly with local irregularities and adapt efficiently to abrupt and small-scale variations in the data. As such, they have been employed for various tasks of filtering, smoothing, and data compression (Zhao & Zhang, 2005; Krommweh, 2010; Fryzlewicz & Timmermans, 2016). The use of wavelets in density estimation has a long history dating back to the 1990s (Cohen, 2003; Härdle *et al.*, 2012; Donoho *et al.*, 1996) and wavelet-based density estimators have been successfully applied to a wide range of observational data (Abramovich *et al.*, 2000; Peter & Rangarajan, 2008; Kang *et al.*, 2013). These well-documented advantages motivate the study of wavelet estimators for the expected persistence diagram.

3 Minimax Density Estimation of the Expected Persistence Diagram

We now present our main results, which are twofold: In our first contribution, we estimate the density of the expected persistence diagram nonparametrically using Haar wavelets and establish its property of minimaxity. In our second contribution, we propose a sparse thresholding wavelet estimator and show its near-minimaxity.

3.1 Framework

Consider a probability distribution P supported on \mathcal{M}^p , and denote the expected persistence diagram associated to P by

$$\mathbf{E}(P) := \mathbb{E}[\mu], \quad (7)$$

where μ is a random variable taking values in the set \mathcal{M}^p distributed according to the law P . Note that, in this context, it is natural to interpret the expected persistence diagram as the Bochner integral of μ .

Our goal is to estimate the Lebesgue density of $\mathbf{E}(P)$ based on N independent and identically distributed (i.i.d.) observations $\{\mu_i\}_{i=1}^N \sim P$. Moreover, we aim to find an estimator which is optimal in the sense of minimax, which we will now define. Here, we use the framework introduced by Divol & Lacombe (2021a).

Definition 4. For $R > 0$, let

$$\Omega_R := \left\{ (t_1, t_2) \in \mathbb{R}^2 : \left| t_1 + R/\sqrt{8} \right| + \left| t_2 - R/\sqrt{8} \right| \leq R/\sqrt{2} \right\}.$$

Denote by $\mathcal{M}_{R,M}^s$ the set of persistence measures $\mu \in \mathcal{M}^s$ that are supported on Ω_R and satisfy $\text{Pers}_s(\mu) \leq M$, where $s \in [0, \infty)$ and $M > 0$. Let $\mathcal{P}_{R,M}^s$ be the set of probability distributions on $\mathcal{M}_{R,M}^s$. The *minimax rate* for estimating $\mathbf{E}(P)$ on $\mathcal{P}_{R,M}^s$ is defined to be

$$\inf_{\hat{\mu}_N} \sup_{P \in \mathcal{P}_{R,M}^s} \mathbb{E} [\text{OT}_p^p(\hat{\mu}_N, \mathbf{E}(P))],$$

where the infimum is taken over all estimators $\hat{\mu}_N$ based on the N i.i.d. samples $\{\mu_i\}_{i=1}^N \sim P$.

Theorem 5 (Lower bound on minimax rate, Theorem 2 in (Divol & Lacombe, 2021a)). *Let $1 \leq p < \infty$, $s \geq 0$, and $M, R > 0$. Then there exists a constant $c_{p,s} > 0$ depending on p and s such that*

$$\inf_{\hat{\mu}_N} \sup_{P \in \mathcal{P}_{R,M}^s} \mathbb{E} [\text{OT}_p^p(\hat{\mu}_N, \mathbf{E}(P))] \geq \frac{c_{p,s} M R^{p-s}}{\sqrt{N}}.$$

Here, the infimum ranges over all possible estimators $\hat{\mu}_N$ that can be computed from the i.i.d. N -sample $\{\mu_i\}_{i=1}^N \sim P$.

Remark 6 (Regularity of density). As noted by Chazal & Divol (2019), the density of the expected persistence diagram is typically smooth. Hence, a natural question to ask is whether the regularity of the density can be leveraged to obtain a faster minimax rate. The answer to this question is negative: in (Divol & Lacombe, 2021a, Theorem 3) it is established that regardless of the assumed regularity on the density, the minimax rate cannot be faster than $1/\sqrt{N}$.

Given the observed N -sample $\{\mu_i\}_{i=1}^N$, a very natural and simple estimator of $\mathbf{E}(P)$ is the *empirical mean* $\bar{\mu}_N$ defined as

$$\bar{\mu}_N := \frac{1}{N} \sum_{i=1}^N \mu_i, \quad (8)$$

which can be computed efficiently. Moreover, the following result states that $\bar{\mu}_N$ achieves the minimax rate.

Theorem 7 (Convergence rate empirical mean, Theorem 1 in (Divol & Lacombe, 2021a)). *Let $1 \leq p < \infty$ and $0 \leq s < p$. Given N i.i.d. samples $\{\mu_i\}_{i=1}^N \sim P$, compute $\bar{\mu}_N$ according to (8). Then*

$$\sup_{P \in \mathcal{P}_{R,M}^s} \mathbb{E} [\text{OT}_p^p(\bar{\mu}_N, \mathbf{E}(P))] \leq c_{p,s} M R^{p-s} a_p(N) \left(\frac{1}{\sqrt{N}} + \frac{1}{N^{p-s}} \right),$$

where $c_{p,s} > 0$ is a constant depending on p and s , and where

$$a_p(N) := \begin{cases} \log_2(N) & \text{if } p = 1, \\ 1 & \text{otherwise.} \end{cases}$$

Thus, whenever $p > 1$ and $p - s \geq 1/2$, we obtain the minimax rate $1/\sqrt{N}$. In particular, this holds under the assumption that the points in the observed persistence diagrams $\{\mu_i\}_{i=1}^N$ are bounded by M , i.e., when we assume $s = 0$.

However, in practice, if we observe N persistence diagrams, the support of $\bar{\mu}_N$ is typically very large since it corresponds to the union of the support of each diagram. This makes the estimator $\bar{\mu}_N$ prohibitive for many applications (Divol & Lacombe, 2021a). Additionally, the estimator $\bar{\mu}_N$ is in general not absolutely continuous with respect to the Lebesgue measure when observing persistence diagrams which are discrete measures.

3.2 Wavelet-Based Estimation

To control transportation distances such as OT_p from above, we construct an explicit coupling (transportation map) between two measures. Indeed, recalling (4), we take the infimum over all couplings to compute OT_p . Thus, using an explicit coupling yields an upper bound. A simple and natural way to construct an efficient transportation map between two measures is to use a multiscale (dyadic) partition of the underlying set (Fournier & Guillin, 2015; Weed & Bach, 2019).

Consider the following multiscale partition of Ω_R : for $k \in \mathbb{N}_0$, define

$$A_k := \left\{ x \in \Omega_R : R 2^{-(k+1)} < \|x - x^\perp\|_2 \leq R 2^{-k} \right\} \text{ such that } \cup_{k \in \mathbb{N}_0} A_k = \Omega_R.$$

Let $J \in \mathbb{N}$, consider the sequence of partitions $\{\mathcal{Q}_{k,j-1}\}_{j=1}^J$ of A_k , where $\mathcal{Q}_{k,j-1}$ consists of squares whose side length is $R 2^{-(k+1)} 2^{-j+1}$ such that $\mathcal{Q}_{k,j}$ is a refinement of $\mathcal{Q}_{k,j-1}$, i.e., for every $Q \in \mathcal{Q}_{k,j}$ there exists a $Q' \in \mathcal{Q}_{k,j-1}$ satisfying $Q \subseteq Q'$. Figure 4 illustrates this multiscale partition.

Intuitively, to construct an explicit transportation map, we recursively apply the following steps for each $k \in \mathbb{N}_0$: given the partition $\mathcal{Q}_{k,0}$, move mass between sets in $\mathcal{Q}_{k,0}$, and then within each set in $\mathcal{Q}_{k,0}$, using the partition $\mathcal{Q}_{k,1}$. This procedure gives the following bound.

Lemma 8 (Lemma 4 in (Divol & Lacombe, 2021a)). *Let $\mu, \nu \in \mathcal{M}^p$ supported on Ω_R , and let $J \in \mathbb{N}$. Then*

$$\begin{aligned} \text{OT}_p^p(\mu, \nu) &\leq 2^{p/2} R^p \sum_{k \geq 0} 2^{-kp} \left(2^{-Jp} (\mu(A_k) \wedge \nu(A_k)) + c_p |\mu(A_k) - \nu(A_k)| \right. \\ &\quad \left. + \sum_{j=1}^J 2^{-jp} \sum_{Q \in \mathcal{Q}_{k,j-1}} |\mu(Q) - \nu(Q)| \right), \end{aligned}$$

where $c_p := 2^{-p/2} (1 + 1/(2^p - 1))$.

Constructing the Wavelet-Based Estimator. We start by recalling the standard Haar system in \mathbb{R}^2 . Denote by χ the characteristic function and let $\tilde{\varphi} := \chi_{[0,1]^2}$. Set

$$\tilde{\varphi}_{j,\ell}(t_1, t_2) := 2^j \tilde{\varphi}(2^j(t_1, t_2) + \ell), \quad (t_1, t_2) \in \mathbb{R}^2, j \in \mathbb{N}_0, \ell = (m, n) \in \mathbb{Z}^2.$$

For $(t_1, t_2) \in \mathbb{R}^2$, define

$$\tilde{\psi}^a(t_1, t_2) := (\chi_{[0,1/2)}(t_1) - \chi_{[1/2,1)}(t_1)) \chi_{[0,1]}(t_2),$$

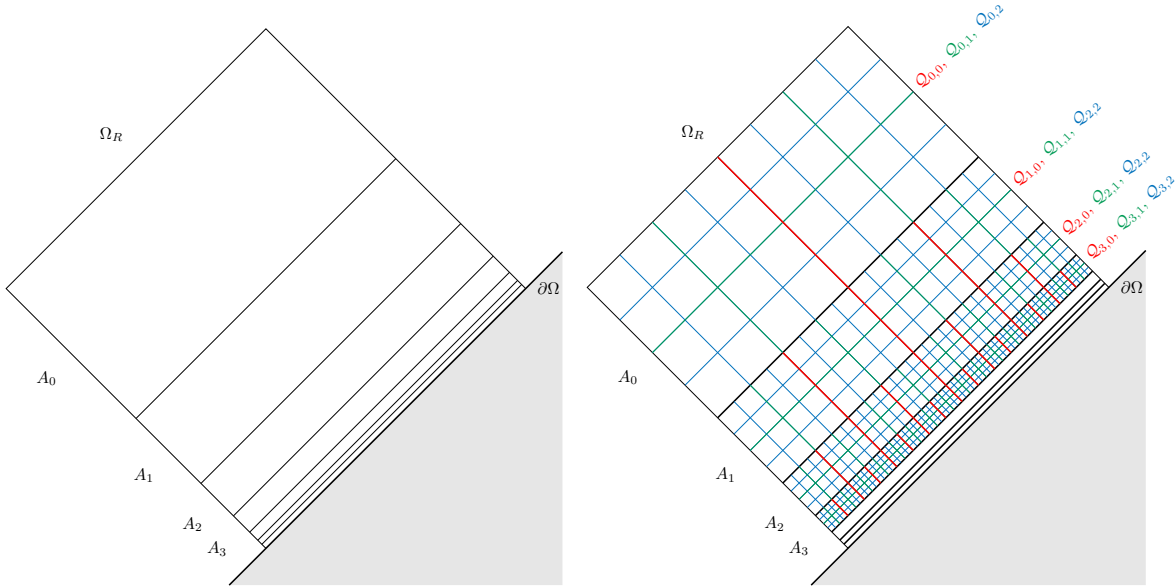


Figure 4: Multiscale partition of Ω_R used to bound OT_p and to construct the wavelet estimator. A similar figure appeared in (Divol & Lacombe, 2021a).

$$\begin{aligned}\tilde{\psi}^b(t_1, t_2) &:= \chi_{[0,1]}(t_1) (\chi_{[0,1/2]}(t_2) - \chi_{[1/2,1]}(t_2)), \\ \tilde{\psi}^c(t_1, t_2) &:= (\chi_{[0,1/2]}(t_1) - \chi_{[1/2,1]}(t_1)) (\chi_{[0,1/2]}(t_2) - \chi_{[1/2,1]}(t_2)),\end{aligned}$$

and set, for $\alpha \in \{a, b, c\}$,

$$\tilde{\psi}_{j,\ell}^\alpha(t_1, t_2) := 2^j \tilde{\psi}^\alpha(2^j(t_1, t_2) + \ell), \quad (t_1, t_2) \in \mathbb{R}^2, j \in \mathbb{N}_0, \ell = (m, n) \in \mathbb{Z}^2.$$

To adapt the Haar system to the geometry of our setup so that the wavelet functions are piecewise constant on the squares of our multiscale partition (see Figure 4), we apply a change of variables. First translate by $1/2$ in the negative t_1 -direction, scale by a factor of R , and finally rotate by $+\pi/4$ to get

$$\mathbb{R}^2 \rightarrow \mathbb{R}^2, \quad \begin{pmatrix} t_1 \\ t_2 \end{pmatrix} \mapsto \begin{pmatrix} u(t_1, t_2) \\ v(t_1, t_2) \end{pmatrix} := \begin{pmatrix} \frac{t_1 + t_2}{\sqrt{2}R} + \frac{1}{2} \\ \frac{t_2 - t_1}{\sqrt{2}R} \end{pmatrix}. \quad (9)$$

Normalizing yields

$$\varphi(t_1, t_2) := R^{-1} \chi_{[0,1]^2}(u(t_1, t_2), v(t_1, t_2)) = R^{-1} \chi_{\Omega_R}(t_1, t_2).$$

The scaled and translated versions of φ then read

$$\varphi_{j,\ell}(t_1, t_2) = 2^j \varphi(2^j t_1 + a_{j,\ell}, 2^j t_2 + b_{j,\ell}), \quad j \in \mathbb{N}_0, \ell = (m, n) \in \mathbb{Z}^2,$$

where $a_{j,\ell} := (m - n - 2^{-1} + 2^{j-1})R/\sqrt{2}$ and $b_{j,\ell} := (m + n - 2^{-1} + 2^{j-1})R/\sqrt{2}$. Moreover,

$$\begin{aligned}\psi^a(t_1, t_2) &:= \frac{1}{R} (\chi_{[0,1/2]}(u(t_1, t_2)) - \chi_{[1/2,1]}(u(t_1, t_2))) \chi_{[0,1]}(v(t_1, t_2)), \\ \psi^b(t_1, t_2) &:= \frac{1}{R} \chi_{[0,1]}(u(t_1, t_2)) (\chi_{[0,1/2]}(v(t_1, t_2)) - \chi_{[1/2,1]}(v(t_1, t_2))), \\ \psi^c(t_1, t_2) &:= \frac{1}{R} (\chi_{[0,1/2]}(u(t_1, t_2)) - \chi_{[1/2,1]}(u(t_1, t_2))) (\chi_{[0,1/2]}(v(t_1, t_2)) - \chi_{[1/2,1]}(v(t_1, t_2))),\end{aligned}$$

and

$$\psi_{j,\ell}^\alpha(t_1, t_2) = 2^j \psi^\alpha(2^j t_1 + a_{j,\ell}, 2^j t_2 + b_{j,\ell}), \quad j \in \mathbb{N}_0, \ell = (m, n) \in \mathbb{Z}^2, \alpha \in \{a, b, c\}. \quad (10)$$

Note that for any $j_0 \in \mathbb{N}_0$, the set

$$\mathcal{V}_{j_0} \cup \bigcup_{j \geq j_0} \mathcal{W}_j$$

is a complete orthonormal system in $L^2(\mathbb{R}^2)$. We thus have the following wavelet expansion for any function $f \in L^2(\mathbb{R}^2)$:

$$f = \sum_{\phi \in \mathcal{V}_{j_0}} \alpha_\phi \phi + \sum_{j \geq j_0} \sum_{\psi \in \mathcal{W}_j} \beta_\psi \psi, \quad (11)$$

where

$$\alpha_\phi := \int_{\mathbb{R}^2} \phi(x) f(x) dx, \quad \phi \in \mathcal{V}_{j_0}, \quad \text{and} \quad \beta_\psi := \int_{\mathbb{R}^2} \psi(x) f(x) dx, \quad \psi \in \mathcal{W}_j, j \geq j_0.$$

That is, the wavelet estimator of an unknown density is constructed by estimating its projection on the wavelet basis. If $f \in L^r(\mathbb{R}^2)$, $1 \leq r < \infty$, the convergence of the infinite sum in (11) holds in $L^r(\mathbb{R}^2)$.

Fix any probability distribution $P \in \mathcal{P}_{R,M}^s$ and let f be the Lebesgue density of $\mathbf{E}(P)$. Given $k \in \mathbb{N}_0$, denote the restriction of f to the set A_k by $f|_{A_k}$, and consider the following wavelet expansion

$$f|_{A_k} = \sum_{\phi \in \mathcal{V}_{k+1}} \alpha_\phi \phi + \sum_{j \geq k+1} \sum_{\psi \in \mathcal{W}_j} \beta_\psi \psi,$$

where $\alpha_\phi = \int_{\Omega_R} \phi(x) f(x) dx$ and $\beta_\psi = \int_{\Omega_R} \psi(x) f(x) dx$. If $f \in L^r(\Omega_R)$, $r \in [1, \infty)$, the convergence also holds in $L^r(\Omega_R)$. Note that since Ω_R is bounded and the functions $\phi \in \mathcal{V}_{k+1}$ and $\psi \in \mathcal{W}_j$ are compactly supported, the sums over \mathcal{V}_{k+1} and \mathcal{W}_j consist of finitely many terms.

Haar Wavelet Estimator. Given N i.i.d. observations $\{\mu_i\}_{i=1}^N \sim P$, we construct the estimator \hat{f} such that

$$\hat{f}|_{A_k} = \sum_{\phi \in \mathcal{V}_{k+1}} \hat{\alpha}_\phi \phi + \sum_{j=k+1}^{J+K} \sum_{\psi \in \mathcal{W}_j} \hat{\beta}_\psi \psi, \quad k \in \{0, 1, \dots, K\}, \quad (12)$$

where $K \in \mathbb{N}_0, J \in \mathbb{N}$ are fixed, and where

$$\hat{\alpha}_\phi = \frac{1}{N} \sum_{i=1}^N \int_{\Omega_R} \phi d\mu_i \quad \text{and} \quad \hat{\beta}_\psi = \frac{1}{N} \sum_{i=1}^N \int_{\Omega_R} \psi d\mu_i.$$

Set $\hat{f}|_{A_k} = 0$ for all $k \geq K+1$.

The function \hat{f} gives the nonparametric Haar wavelet estimator. Its construction is based on a truncation of the series expansion onto the wavelet basis; the coefficients of the expansion are set through an empirical estimate. We will denote by $\hat{\mu}_H$ the measure with Lebesgue density \hat{f} .

We have now introduced all the required quantities in order to state our first main result, namely, the minimaxity of the Haar wavelet estimator.

Theorem 9 (Minimaxity of the Haar wavelet estimator). *Let P be a probability distribution supported on $\mathcal{M}_{M,R}^s$ such that the Lebesgue density f of $\mathbf{E}(P)$ satisfies*

$$\|f\|_{L^\infty(A_k)} \leq C^2 M R^{-s} 2^{ks}, \quad k \in \mathbb{N}_0, \text{ for some } C > 0,$$

and let $1 \leq p < \infty$, $0 \leq s < p$. Then, for $\hat{\mu}_H$ with $J = K = \lceil \log_2(N) \rceil$,

$$\mathbb{E} [\text{OT}_p^p(\hat{\mu}_H, \mathbf{E}(P))] \leq c_{p,s} M R^{p-s} \left(\frac{R}{N^p} + \frac{C R a_p(N)}{\sqrt{N}} + \frac{1}{N^{p-s}} \right),$$

where $c_{p,s}$ is a constant depending only on p and s , and where

$$a_p(N) := \begin{cases} \log_2(N) & \text{if } p = 1, \\ 1 & \text{otherwise.} \end{cases}$$

Remark 10 (Discussion of assumption). Note that the condition on the probability distribution P holds in particular if the Lebesgue density f belongs to the class of ℓ -times continuously differentiable functions, C^ℓ , $\ell \in \mathbb{N}_0$. It is shown in (Chazal & Divol, 2019, Theorem 3.5) that $f \in C^\ell$ if the underlying dataset admits a density of class C^ℓ with respect to the Hausdorff measure. This means that whenever the data points are sampled in a smooth manner, f will exhibit the same regularity. Also, note that the minimax rate cannot be faster than $1/\sqrt{N}$ irrespective of the regularity assumed on the EPD as previously mentioned; see Remark 6.

To prove Theorem 9, we require the following property of the EPD, which is a consequence of the linearity of expectation.

Lemma 11. *Let $\mu \sim P$. Then, for every measurable function g ,*

$$\mathbb{E} \left[\int_{\Omega_R} g \, d\mu \right] = \int_{\Omega_R} g \, d\mathbf{E}(P).$$

Proof. First, suppose that g is a simple function, i.e., $g = \sum_{k=1}^n b_k \chi_{B_k}$, where $n \in \mathbb{N}$, $\{b_k\}_{k=1}^n \subset \mathbb{R}$, and where $\{B_k\}_{k=1}^n \subset \Omega_R$ is a sequence of Borel sets. We obtain

$$\begin{aligned} \mathbb{E} \left[\int_{\Omega_R} g \, d\mu \right] &= \mathbb{E} \left[\int_{\Omega_R} \sum_{k=1}^n b_k \chi_{B_k} \, d\mu \right] \\ &= \sum_{k=1}^n b_k \mathbb{E} \left[\int_{\Omega_R} \chi_{B_k} \, d\mu \right] \end{aligned} \tag{13}$$

$$\begin{aligned} &= \sum_{k=1}^n b_k \mathbb{E} [\mu(B_k)] \\ &= \sum_{k=1}^n b_k \mathbb{E} [\mu] (B_k) \end{aligned} \tag{14}$$

$$\begin{aligned} &= \sum_{k=1}^n b_k \int_{\Omega_R} \chi_{B_k} \, d\mathbf{E}(P) \\ &= \int_{\Omega_R} \sum_{k=1}^n b_k \chi_{B_k} \, d\mathbf{E}(P) \\ &= \int_{\Omega_R} g \, d\mathbf{E}(P), \end{aligned} \tag{15}$$

where (13) follows from linearity; (14) holds by Definition 3; and in (15), we utilized (7).

Finally, using the monotone convergence theorem, the desired result can be established for any measurable function g . \square

We are now ready to prove Theorem 9. The key in this proof is first to decompose the Lebesgue density, f , of $\mathbf{E}(P)$ according to the multiscale partition illustrated in Figure 4 and then to bound the distance between the estimator \hat{f} and f on each dyadic square.

Proof of Theorem 9. Let the Haar wavelet expansion of the Lebesgue density of $\mathbf{E}(P)$ be given by

$$f|_{A_k} = \sum_{\phi \in \mathcal{V}_{k+1}} \alpha_\phi \phi + \sum_{j \geq k+1} \sum_{\psi \in \mathcal{W}_j} \beta_\psi \psi, \quad k \in \mathbb{N}_0, \quad (16)$$

where $\alpha_\phi = \int_{\Omega_R} \phi d\mathbf{E}(P)$ and $\beta_\psi = \int_{\Omega_R} \psi d\mathbf{E}(P)$.

Apply Lemma 8 to the measures $\hat{\mu}_H$ and $\mathbf{E}(P)$, and split the sum over k into two parts to obtain

$$\text{OT}_p^p(\hat{\mu}_H, \mathbf{E}(P)) \leq S_1 + S_2, \quad (17)$$

where S_1 contains the first $K + 1$ terms and S_2 the remaining terms:

$$\begin{aligned} S_1 := & 2^{p/2} R^p \sum_{k=0}^K 2^{-kp} \left(2^{-Jp} (\hat{\mu}_H(A_k) \wedge \mathbf{E}(P)(A_k)) + c_p |\hat{\mu}_H(A_k) - \mathbf{E}(P)(A_k)| \right. \\ & \left. + \sum_{j=1}^J 2^{-jp} \sum_{Q \in \mathcal{Q}_{k,j-1}} |\hat{\mu}_H(Q) - \mathbf{E}(P)(Q)| \right), \end{aligned} \quad (18)$$

$$\begin{aligned} S_2 := & 2^{p/2} R^p \sum_{k \geq K+1} 2^{-kp} \left(2^{-Jp} (\hat{\mu}_H(A_k) \wedge \mathbf{E}(P)(A_k)) + c_p |\hat{\mu}_H(A_k) - \mathbf{E}(P)(A_k)| \right. \\ & \left. + \sum_{j=1}^J 2^{-jp} \sum_{Q \in \mathcal{Q}_{k,j-1}} |\hat{\mu}_H(Q) - \mathbf{E}(P)(Q)| \right). \end{aligned} \quad (19)$$

The proof may be divided into three steps. In Step 1 and Step 2, we will estimate S_1 and S_2 in expectation, respectively. The desired result will be established in Step 3.

Step 1 (Estimation of S_1). Let $k \in \{0, 1, \dots, K\}$. First observe that for $Q \in \mathcal{Q}_{k,j-1}$ with $j \geq 1$, $R^{-1}2^{k+j}\chi_Q \in \mathcal{V}_{k+j}$. Since $\mathcal{V}_{k+j} \cup \bigcup_{j' \geq k+j} \mathcal{W}_{j'}$ forms an orthonormal system in $L^2(\mathbb{R}^2)$, it holds that

$$\int_Q \psi dx = \int_{\mathbb{R}^2} \chi_Q \psi dx = 0, \quad \text{for all } \psi \in \bigcup_{j' \geq k+j} \mathcal{W}_{j'}. \quad (20)$$

Therefore, we have, for $Q \in \mathcal{Q}_{k,j-1}$ with $2 \leq j \leq J$,

$$|\hat{\mu}_H(Q) - \mathbf{E}(P)(Q)| = \left| \sum_{\phi \in \mathcal{V}_{k+1}} (\hat{\alpha}_\phi - \alpha_\phi) \int_Q \phi dx + \sum_{j'=k+1}^{k+j-1} \sum_{\psi \in \mathcal{W}_{j'}} (\hat{\beta}_\psi - \beta_\psi) \int_Q \psi dx \right| \quad (21)$$

$$\begin{aligned} & \leq \sum_{\phi \in \mathcal{V}_{k+1}} |\hat{\alpha}_\phi - \alpha_\phi| \int_Q \phi dx + \sum_{j'=k+1}^{k+j-1} \sum_{\psi \in \mathcal{W}_{j'}} |\hat{\beta}_\psi - \beta_\psi| \int_Q |\psi| dx \\ & \leq R^{-1}|Q| \left(\sum_{\substack{\phi \in \mathcal{V}_{k+1} \\ \text{supp}(\phi) \supseteq Q}} 2^{k+1} |\hat{\alpha}_\phi - \alpha_\phi| + \sum_{j'=k+1}^{k+j-1} \sum_{\substack{\psi \in \mathcal{W}_{j'} \\ \text{supp}(\psi) \supseteq Q}} 2^{j'} |\hat{\beta}_\psi - \beta_\psi| \right), \end{aligned} \quad (22)$$

where we used in (21) the wavelet expansions (12) and (16) as well as the orthogonality relation (20); and where (22) holds because $\|\phi\|_{L^\infty(\mathbb{R}^2)} = R^{-1}2^{k+1}$ for $\phi \in \mathcal{V}_{k+1}$, $\|\psi\|_{L^\infty(\mathbb{R}^2)} = R^{-1}2^{j'}$ for $\psi \in \mathcal{W}_{j'}$, and $|Q| = \int_Q dx$. Note that, for $Q \in \mathcal{Q}_{k,0}$, $R^{-1}2^{k+j}\chi_Q \in \mathcal{V}_{k+1}$ so that, by (20), $\int_Q \psi dx = 0$ for all $\psi \in \mathcal{W}_{j'}$ with $j' \geq k+1$. Thus, whenever $Q \in \mathcal{Q}_{k,0}$, it holds that

$$|\hat{\mu}_H(Q) - \mathbf{E}(P)(Q)| = \left| \sum_{\phi \in \mathcal{V}_{k+1}} (\hat{\alpha}_\phi - \alpha_\phi) \int_Q \phi dx \right| \leq R^{-1}2^{k+1}|Q| \sum_{\substack{\phi \in \mathcal{V}_{k+1} \\ \text{supp}(\phi) \supseteq Q}} |\hat{\alpha}_\phi - \alpha_\phi|.$$

Next, we will derive an upper bound for the expected error of the wavelet coefficients. To this end, let $\mu \sim P$. Because $\{\mu_i\}_{i=1}^N \sim P$ are i.i.d., we obtain, using [Lemma 11](#), the following identity:

$$\begin{aligned}
\mathbb{E} \left[(\hat{\alpha}_\phi - \alpha_\phi)^2 \right] &= \mathbb{E} \left[\left(\frac{1}{N} \sum_{i=1}^N \int_{\Omega_R} \phi \, d\mu_i - \int_{\Omega_R} \phi \, d\mathbf{E}(P) \right)^2 \right] \\
&= \mathbb{E} \left[\frac{1}{N^2} \sum_{i=1}^N \sum_{j=1}^N \int_{\Omega_R} \phi \, d\mu_i \int_{\Omega_R} \phi \, d\mu_j - \frac{2}{N} \sum_{i=1}^N \int_{\Omega_R} \phi \, d\mu_i \int_{\Omega_R} \phi \, d\mathbf{E}(P) + \left(\int_{\Omega_R} \phi \, d\mathbf{E}(P) \right)^2 \right] \\
&= \frac{1}{N} \mathbb{E} \left[\left(\int_{\Omega_R} \phi \, d\mu \right)^2 \right] + \frac{N-1}{N} \left(\int_{\Omega_R} \phi \, d\mathbf{E}(P) \right)^2 - \left(\int_{\Omega_R} \phi \, d\mathbf{E}(P) \right)^2 \\
&= \frac{1}{N} \left(\mathbb{E} \left[\left(\int_{\Omega_R} \phi \, d\mu \right)^2 \right] - \left(\int_{\Omega_R} \phi \, d\mathbf{E}(P) \right)^2 \right).
\end{aligned}$$

Applying Jensen's inequality yields

$$\mathbb{E} \left[|\hat{\alpha}_\phi - \alpha_\phi| \right] \leq \sqrt{\frac{\text{Var}(\int_{\Omega_R} \phi \, d\mu)}{N}} \leq \sqrt{\frac{\mathbb{E} \left[\left(\int_{\Omega_R} \phi \, d\mu \right)^2 \right]}{N}}. \quad (23)$$

Likewise,

$$\mathbb{E} \left[|\hat{\beta}_\psi - \beta_\psi| \right] \leq \sqrt{\frac{\text{Var}(\int_{\Omega_R} \psi \, d\mu)}{N}} \leq \sqrt{\frac{\mathbb{E} \left[\left(\int_{\Omega_R} \psi \, d\mu \right)^2 \right]}{N}}. \quad (24)$$

To bound the second moment $\mathbb{E} \left[\left(\int_{\Omega_R} \phi \, d\mu \right)^2 \right]$, we may assume $\mu(\text{supp}(\phi)) > 0$ almost surely; indeed, otherwise $\mathbb{E} \left[\left(\int_{\Omega_R} \phi \, d\mu \right)^2 \right] = 0$. We then get:

$$\begin{aligned}
\mathbb{E} \left[\left(\int_{\Omega_R} \phi \, d\mu \right)^2 \right] &= \mathbb{E} \left[\left(\int_{\text{supp}(\phi)} \phi \, d\mu \right)^2 \right] \\
&= \mathbb{E} \left[\mu(\text{supp}(\phi))^2 \left(\int_{\text{supp}(\phi)} \phi \frac{d\mu}{\mu(\text{supp}(\phi))} \right)^2 \right] \\
&\leq \mathbb{E} \left[\mu(\text{supp}(\phi))^2 \int_{\text{supp}(\phi)} \phi^2 \frac{d\mu}{\mu(\text{supp}(\phi))} \right] \quad (25)
\end{aligned}$$

$$\leq MR^{-s} 2^{ks} \mathbb{E} \left[\int_{\text{supp}(\phi)} \phi^2 \, d\mu \right] \quad (26)$$

$$= MR^{-s} 2^{ks} \int_{\text{supp}(\phi)} \phi^2 \, d\mathbf{E}(P) \quad (27)$$

$$\begin{aligned}
&= MR^{-s} 2^{ks} \int_{\text{supp}(\phi)} \phi^2 f \, dx \\
&\leq MR^{-s} 2^{ks} \|f\|_{L^\infty(A_k)} \int_{\text{supp}(\phi)} \phi^2 \, dx \\
&= MR^{-s} 2^{ks} \|f\|_{L^\infty(A_k)}
\end{aligned}$$

$$\leq (CMR^{-s} 2^{ks})^2, \quad (28)$$

where (25) follows from Jensen's inequality; in (26) we used that $\text{supp}(\phi) \subset A_k$ and the following fact stated in (Divol & Lacombe, 2021a, (A.5)): for any $\mu \in \mathcal{M}_{M,R}^s$,

$$\mu(B) = \int_B \frac{\text{dist}(x, \partial\Omega)^s}{\text{dist}(x, \partial\Omega)^s} d\mu(x) \leq MR^{-s}2^{ks}, \quad \text{for all } B \subseteq A_k; \quad (29)$$

the identity (27) is due to Lemma 11; and where (28) holds based on our assumption that $\|f\|_{L^\infty(A_k)} \leq C^2MR^{-s}2^{ks}$. Likewise,

$$\mathbb{E} \left[\left(\int_{\Omega_R} \psi d\mu \right)^2 \right] \leq (CMR^{-s}2^{ks})^2. \quad (30)$$

Now observe that $\text{card}(\{\phi \in \mathcal{V}_{k+1} : \text{supp}(\phi) \supseteq Q\}) = 1$ for all $Q \in \mathcal{Q}_{k,j-1}$ with $j \geq 1$. Thanks to (23) and (28), we have

$$\sum_{\substack{\phi \in \mathcal{V}_{k+1} \\ \text{supp}(\phi) \supseteq Q}} 2^{k+1} \mathbb{E} [|\hat{\alpha}_\phi - \alpha_\phi|] \leq \sum_{\substack{\phi \in \mathcal{V}_{k+1} \\ \text{supp}(\phi) \supseteq Q}} 2^{k+1} \sqrt{\frac{\mathbb{E} \left[\left(\int_{\Omega_R} \phi d\mu \right)^2 \right]}{N}} \leq \frac{CMR^{-s}2^{k(s+1)+1}}{\sqrt{N}}. \quad (31)$$

Similarly, since $\text{card}(\{\psi \in \mathcal{W}_{j'} : \text{supp}(\psi) \supseteq Q\}) = 3$ (see (10)), it follows from (24) and (30) that

$$\sum_{\substack{\psi \in \mathcal{W}_{j'} \\ \text{supp}(\psi) \supseteq Q}} \mathbb{E} [|\hat{\beta}_\psi - \beta_\psi|] \leq \sum_{\substack{\psi \in \mathcal{W}_{j'} \\ \text{supp}(\psi) \supseteq Q}} \sqrt{\frac{\mathbb{E} \left[\left(\int_{\Omega_R} \psi d\mu \right)^2 \right]}{N}} \leq \frac{3CMR^{-s}2^{ks}}{\sqrt{N}}.$$

Using $\sum_{j'=k+1}^{k+j-1} 2^{j'} \leq 2^{k+j}$, we obtain

$$\sum_{j'=k+1}^{k+j-1} \sum_{\substack{\psi \in \mathcal{W}_{j'} \\ \text{supp}(\psi) \supseteq Q}} 2^{j'} \mathbb{E} [|\hat{\beta}_\psi - \beta_\psi|] \leq \frac{3CMR^{-s}2^{k(s+1)+j}}{\sqrt{N}}. \quad (32)$$

Substituting (31) and (32) into (22) yields

$$\mathbb{E} [|\hat{\mu}_H(Q) - \mathbf{E}(P)(Q)|] \leq \frac{|Q|}{\sqrt{N}} CMR^{-s-1}2^{k(s+1)+1} (1 + 3 \cdot 2^{j-1}). \quad (33)$$

Since $\mathcal{Q}_{k,j-1}$ is a partition of A_k and $|A_k| = R^22^{-(k+1)}$, we get, by summing (33) over all $Q \in \mathcal{Q}_{k,j-1}$, for $j \geq 2$,

$$\begin{aligned} \sum_{Q \in \mathcal{Q}_{k,j-1}} \mathbb{E} [|\hat{\mu}_H(Q) - \mathbf{E}(P)(Q)|] &\leq \frac{|A_k|}{\sqrt{N}} CMR^{-s-1}2^{k(s+1)+1} (1 + 3 \cdot 2^{j-1}) \\ &= \frac{1}{\sqrt{N}} CMR^{-s+1}2^{ks} (1 + 3 \cdot 2^{j-1}). \end{aligned} \quad (34)$$

When $j = 1$,

$$\sum_{Q \in \mathcal{Q}_{k,j-1}} \mathbb{E} [|\hat{\mu}_H(Q) - \mathbf{E}(P)(Q)|] \leq \frac{|A_k|}{\sqrt{N}} CMR^{-s-1}2^{k(s+1)+1} = \frac{1}{\sqrt{N}} CMR^{-s+1}2^{ks}. \quad (35)$$

Moreover, since

$$|\hat{\mu}_H(A_k) - \mathbf{E}(P)(A_k)| = \left| \sum_{Q \in \mathcal{Q}_{k,0}} \hat{\mu}_H(Q) - \mathbf{E}(P)(Q) \right|,$$

it follows from (35) that

$$\mathbb{E} [|\hat{\mu}_H(A_k) - \mathbf{E}(P)(A_k)|] \leq \frac{1}{\sqrt{N}} C M R^{-s+1} 2^{ks}. \quad (36)$$

Thanks to (29), we also have

$$\hat{\mu}_H(A_k) \wedge \mathbf{E}(P)(A_k) \leq M R^{-s} 2^{ks}. \quad (37)$$

Using the estimates (34) to (37) we can bound S_1 , defined in (18), in expectation:

$$\begin{aligned} \mathbb{E}[S_1] &\leq 2^{p/2} M R^{p-s+1} \sum_{k=0}^K 2^{-k(p-s)} \left(2^{-Jp} + c_p \frac{C}{\sqrt{N}} + \sum_{j=1}^J 2^{-jp} \left(\frac{C(1+3 \cdot 2^{j-1})}{\sqrt{N}} \right) \right) \\ &\leq 2^{p/2} M R^{p-s+1} \sum_{k=0}^K 2^{-k(p-s)} \left(2^{-Jp} + c_p \frac{C}{\sqrt{N}} + \frac{2C}{\sqrt{N}} \sum_{j=1}^J 2^{-j(p-1)} \right). \end{aligned} \quad (38)$$

Step 2 (Estimation of S_2). Let $k \geq K+1$. Note that, by definition, $\hat{\mu}_H(B) = 0$ for any $B \subseteq A_k$. Thanks to (29), we get

$$\sum_{Q \in \mathcal{Q}_{k,j-1}} |\hat{\mu}_H(Q) - \mathbf{E}(P)(Q)| = \sum_{Q \in \mathcal{Q}_{k,j-1}} \mathbf{E}(P)(Q) = \mathbf{E}(P)(A_k) \leq M R^{-s} 2^{ks}, \quad (39)$$

$$|\hat{\mu}_H(A_k) - \mathbf{E}(P)(A_k)| \leq M R^{-s} 2^{ks}, \quad (40)$$

and

$$\hat{\mu}_H(A_k) \wedge \mathbf{E}(P)(A_k) = 0. \quad (41)$$

Hence, substituting the estimates (39) to (41) into (19) gives

$$\begin{aligned} S_2 &\leq 2^{p/2} R^p \sum_{k \geq K+1} 2^{-kp} \left(c_p M R^{-s} 2^{ks} + \sum_{j=1}^J 2^{-jp} M R^{-s} 2^{ks} \right) \\ &\leq 2^{p/2} (c_p + 1/(2^p - 1)) M R^{p-s} \sum_{k \geq K+1} 2^{-k(p-s)} \\ &= c'_p M R^{p-s} \sum_{k \geq K+1} 2^{-k(p-s)} \\ &= c'_p M R^{p-s} \frac{2^{-(p-s)K}}{2^{p-s} - 1}, \end{aligned} \quad (42)$$

where $c'_p := 2^{p/2} (c_p + 1/(2^p - 1)) = (2^{p/2} + 2^p)/(2^p - 1)$.

Step 3. Finally, combining (17), (38) and (42) results in

$$\begin{aligned} &\mathbb{E} [\text{OT}_p^p(\hat{\mu}_H, \mathbf{E}(P))] \\ &\leq 2^{p/2} M R^{p-s+1} \sum_{k=0}^K 2^{-k(p-s)} \left(2^{-Jp} + c_p \frac{C}{\sqrt{N}} + \frac{2C}{\sqrt{N}} \sum_{j=1}^J 2^{-j(p-1)} \right) + c'_p M R^{p-s} \frac{2^{-(p-s)K}}{2^{p-s} - 1}. \end{aligned}$$

Setting $K = \lceil \log_2(N) \rceil$ and $J = \lceil \log_2(N) \rceil$ yields the desired estimate

$$\mathbb{E} [\text{OT}_p^p(\hat{\mu}_H, \mathbf{E}(P))] \leq c_{p,s} M R^{p-s} \left(\frac{R}{N^p} + \frac{C R a_p(N)}{\sqrt{N}} + \frac{1}{N^{p-s}} \right),$$

where $c_{p,s}$ is a constant depending only on p and s . \square

Theorem 9 also provides an estimate of the optimal rate of convergence of the Haar wavelet estimator, defined up to constants and variable factors depending on s and p which stay bounded.

Thresholding Haar Wavelet Estimator. We now turn to our practical contribution, which entails a class of nonparametric density estimators and uses a Haar wavelet basis that discards small coefficients by introducing a threshold below which coefficients are set to zero (hard thresholding). The threshold is set following the procedure proposed in (Donoho *et al.*, 1996), where it was designed to attain exactly or approximately optimal convergence rates.

Consider the following hard thresholding technique: fix $\tau > 0$ and let

$$\tau_j := CMR^{-s}\tau 2^{j/p} \frac{j}{\sqrt{N}}.$$

For any $\psi \in \mathcal{W}_j$, consider

$$\tilde{\beta}_\psi := \begin{cases} \hat{\beta}_\psi & \text{if } |\hat{\beta}_\psi| > \tau_j, \\ 0 & \text{otherwise.} \end{cases}$$

Construct the estimator \tilde{f} according to

$$\tilde{f}|_{A_k} = \sum_{\phi \in \mathcal{V}_{k+1}} \hat{\alpha}_\phi \phi + \sum_{j=k+1}^{J+K} \sum_{\psi \in \mathcal{W}_j} \tilde{\beta}_\psi \psi, \quad k \in \{0, 1, \dots, K\},$$

and $\tilde{f}|_{A_k} = 0$, $k \geq K+1$. The function \tilde{f} represents the thresholding Haar wavelet estimator as first proposed by Donoho *et al.* (1996). Let $\tilde{\mu}_H$ be the measure whose Lebesgue density is \tilde{f} .

Corollary 12 (Near-optimal minimaxity of the thresholding Haar wavelet estimator). *Under the assumptions of Theorem 9, we have that*

$$\mathbb{E} [\text{OT}_p^p(\tilde{\mu}_H, \mathbf{E}(P))] \leq \tilde{c}_{p,s} MR^{p-s} \left(\frac{R}{N^p} + \frac{CRa_p(N)}{\sqrt{N}} + \frac{CR\tau \log_2(N)}{\sqrt{N}} + \frac{1}{N^{p-s}} \right),$$

where $\tilde{c}_{p,s}$ is a constant depending only on p and s , and where

$$a_p(N) := \begin{cases} \log_2(N) & \text{if } p = 1, \\ 1 & \text{otherwise.} \end{cases}$$

Proof. Let $\psi \in \mathcal{W}_{j'}$. Using the triangle inequality, we compute

$$\begin{aligned} \mathbb{E} [|\tilde{\beta}_\psi - \beta_\psi|] &\leq \mathbb{E} [|\tilde{\beta}_\psi - \hat{\beta}_\psi| + |\hat{\beta}_\psi - \beta_\psi|] \\ &= \mathbb{E} [|\hat{\beta}_\psi| \mathbb{1}_{\{|\hat{\beta}_\psi| \leq \tau_{j'}\}} + |\beta_\psi - \hat{\beta}_\psi|] \\ &\leq \tau_{j'} + \mathbb{E} [|\beta_\psi - \hat{\beta}_\psi|]. \end{aligned}$$

Thus,

$$\begin{aligned} \sum_{j'=k+1}^{k+j-1} \sum_{\substack{\psi \in \mathcal{W}_{j'} \\ \text{supp}(\psi) \supseteq Q}} 2^{j'} \mathbb{E} [|\tilde{\beta}_\psi - \beta_\psi|] &\leq \sum_{j'=k+1}^{k+j-1} \sum_{\substack{\psi \in \mathcal{W}_{j'} \\ \text{supp}(\psi) \supseteq Q}} 2^{j'} \left(\mathbb{E} [|\beta_\psi - \hat{\beta}_\psi|] + \tau_{j'} \right) \\ &\leq \frac{3CMR^{-s}2^{k(s+1)+j}}{\sqrt{N}} + 3 \sum_{j'=k+1}^{k+j-1} 2^{j'} \tau_{j'}, \end{aligned} \quad (43)$$

where we used (32) and $\text{card}(\{\psi \in \mathcal{W}_{j'} : \text{supp}(\psi) \supseteq Q\}) = 3$ in the last inequality. Computing

$$\sum_{j'=k+1}^{k+j-1} 2^{j'} \tau_{j'} \leq CMR^{-s}\tau 2^{(k+j)/p} \frac{j+k}{\sqrt{N}}$$

and substituting this into (43), we get

$$\sum_{j'=k+1}^{k+j-1} \sum_{\substack{\psi \in \mathcal{W}_{j'} \\ \text{supp}(\psi) \supseteq Q}} 2^{j'} \mathbb{E} \left[\left| \tilde{\beta}_\psi - \beta_\psi \right| \right] \leq \frac{3CMR^{-s} (2^{k(s+1)+j} + \tau(k+j)2^{(j+k)/p})}{\sqrt{N}}. \quad (44)$$

The remainder of this proof follows exactly the same steps as in the proof of [Theorem 9](#), where we replace $\hat{\mu}_H$ by $\tilde{\mu}_H$ and where (44) plays the role of (32). \square

Thus, the thresholding Haar wavelet estimator achieves near-optimal rates. Because of the truncation, only a few wavelet coefficients are nonzero and contribute to the estimator \tilde{f} . Therefore, \tilde{f} can be considered as a *sparse* representation of the expected persistence diagram $\mathbf{E}(P)$. This is in contrast to the empirical mean $\bar{\mu}_N$ whose support tends to be very large. The sparsity of the thresholding Haar wavelet estimator has been leveraged for data compression in several contexts ([Krommweh, 2010](#); [Fryzlewicz & Timmermans, 2016](#)) and may be more practical in TDA applications where the use of $\bar{\mu}_N$ may be restrictive due to its large support.

4 Numerical Experiments

We will now verify our theoretical results established in [Section 3](#) by numerical experiments and illustrate the practical use of the presented estimation techniques in a classification problem in the context of dynamical systems. Here, persistent homology is computed using the `GUDHI` library ([The GUDHI Project, 2015](#)) as well as the `giotto-tda` library ([Tauzin *et al.*, 2020](#)) for `Python`. The implementation of the optimal partial transport metric is based on tools from the `POT` library ([Flamary *et al.*, 2021](#)) for `Python`.

4.1 Convergence Rates: Three Examples

To investigate the convergence rates of the aforementioned estimators, we need to compute $\text{OT}_p(\hat{\mu}_N, \mathbf{E}(P))$, where $\hat{\mu}_N$ is an arbitrary estimator. Note, however, that the (true) expected persistence diagram cannot be computed explicitly in general. A closed-form solution of the expected persistence diagram is known for only a few examples ([Divol & Lacombe, 2021a](#)). To deal with this issue, we approximate $\text{OT}_p(\hat{\mu}_N, \mathbf{E}(P))$ by $\text{OT}_p(\hat{\mu}_N, \bar{\mu}_M)$, where $\bar{\mu}_M = \frac{1}{M} \sum_{i=1}^M \mu_i$, and where M is significantly larger than N , assuming we have access to M samples.

We study three datasets, the torus and double torus, as well as a clustered process.

Torus. We observe the point clouds $\{X_i\}_{i=1}^M$, $M = 10,000$, consisting of $n = 1000$ points which are sampled from a torus with inner radius 0.5, outer radius 2 perturbed by additive Gaussian noise with variance 0.5. We compute the persistence diagrams $\{\mu_i\}_{i=1}^M$.

The convergence rates of the Haar wavelet estimator $\hat{\mu}_H$ are shown in [Figure 5](#) for $p \in \{1, 2, 3, 4\}$, where $\bar{\mu}_N$ is based on N samples from $\{\mu_i\}_{i=1}^M$, and where N takes values between 10 and 500. We obtain the convergence rates predicted by [Theorem 9](#), namely $1/\sqrt{N}$ for $p > 1$ and $\log_2(N)/\sqrt{N}$ for $p = 1$.

Evaluating the convergence behavior of the thresholding Haar wavelet estimator for $\tau \in \{5, 10, 15\}$ (see [Figure 6](#)), we deduce that the obtained rates are consistent with [Corollary 12](#); namely, we get a rate of $\log_2(N)/\sqrt{N}$ for each $\tau \in \{5, 10, 15\}$. From [Table 1](#) it becomes apparent that thresholding significantly reduces the number of nonzero wavelet coefficients. In particular, we have a compression rate of up to 99% compared to the Haar wavelet estimator ($\tau = 0$). In addition, we can observe that describing the estimator $\bar{\mu}_N$ requires substantially more information (as quantified by the cardinality of its support) than the thresholding Haar wavelet estimators, making the latter more convenient in applications where, for example, fast subsequent computations are required or storage is limited.

Notice that there is a trade-off between sparsity and convergence rate of the (thresholding) Haar wavelet estimator: a very sparse estimator entails an extra factor of $\log_2(N)$ in terms of convergence rate (see the $\tau > 0$ compared to $\tau = 0$ curves in [Figure 6](#)). Also, note that the error $\text{OT}_p^p(\tilde{\mu}_H, \bar{\mu}_M)$ increases as τ gets larger, i.e., with a more stringent thresholding of the wavelets coefficients, the approximation becomes increasingly coarse, compromising accuracy.

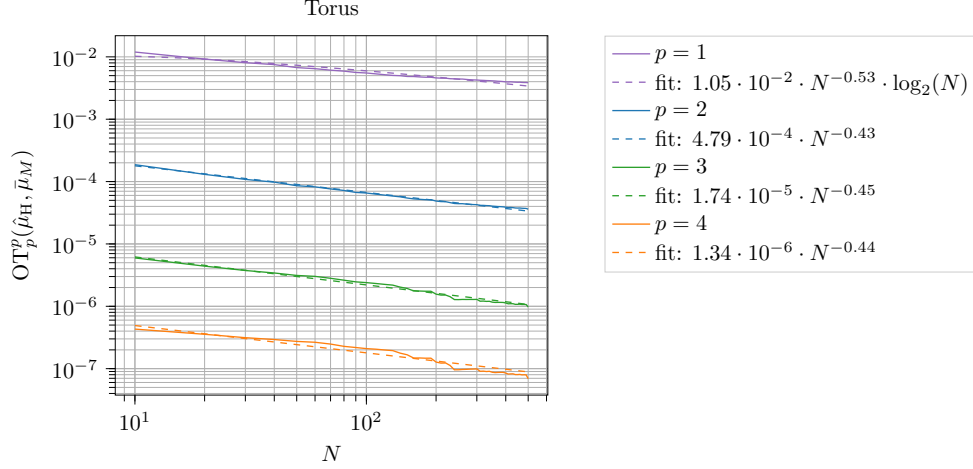


Figure 5: Convergence rates of the Haar wavelet estimator $\hat{\mu}_H$, averaged over 10 iterations, for different sample sizes N ranging from 10 to 500. We take $N \mapsto a \cdot N^{-b} \cdot \log_2(N)$ as a model function (dashed line) for $p = 1$ and $N \mapsto a \cdot N^{-b}$ for $p > 1$, where $a, b \in \mathbb{R}$ are the parameters to fit.

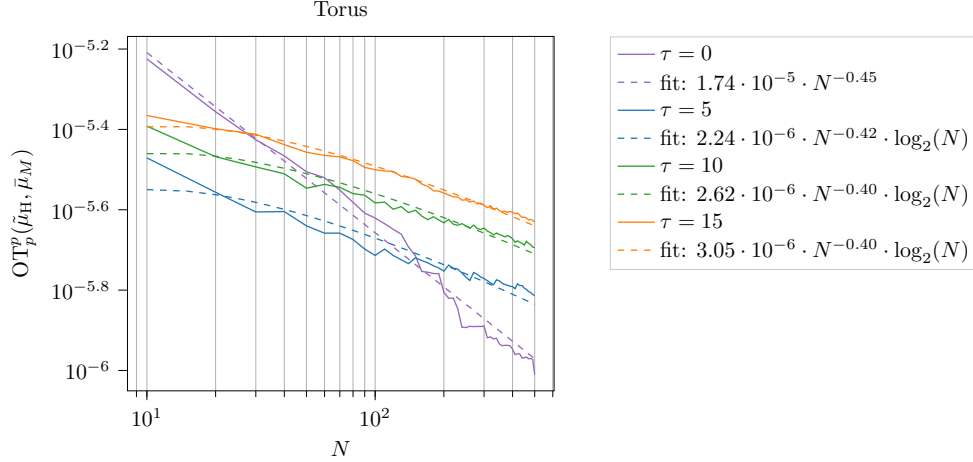


Figure 6: Convergence rates of the thresholding Haar wavelet estimator $\tilde{\mu}_H$, averaged over 10 iterations, where $N \in \{10, \dots, 500\}$ and $p = 3$. We consider the model function (dashed line) $N \mapsto a \cdot N^{-b} \cdot \log_2(N)$ whenever $\tau > 0$ with $a, b \in \mathbb{R}$ being the model parameters.

	$N = 100$	$N = 300$	$N = 500$
Support of $\bar{\mu}_N$	456,900	1,370,700	2,284,500
Nonzero $\tilde{\mu}_H$ coefficients, $\tau = 0$	272,206	370,999	420,456
Nonzero $\tilde{\mu}_H$ coefficients, $\tau = 5$	20,000 (c.r. $\approx 93\%$)	21,101 (c.r. $\approx 94\%$)	21,930 (c.r. $\approx 95\%$)
Nonzero $\tilde{\mu}_H$ coefficients, $\tau = 10$	7,602 (c.r. $\approx 97\%$)	8,280 (c.r. $\approx 98\%$)	9,056 (c.r. $\approx 98\%$)
Nonzero $\tilde{\mu}_H$ coefficients, $\tau = 15$	4,668 (c.r. $\approx 98\%$)	5,571 (c.r. $\approx 98\%$)	6,154 (c.r. $\approx 99\%$)

Table 1: Cardinality of the support set of the empirical mean $\bar{\mu}_N$ and the number of nonzero coefficients of $\tilde{\mu}_H$, $\tau \in \{0, 5, 10, 15\}$, averaged over 10 runs, for different sample sizes N . The corresponding compression rates (c.r.) from thresholding ($\tau > 0$) compared to the case $\tau = 0$ are provided in brackets.

In Figure 7, we see that for low τ , the estimated density contains fine details, due to the presence of many small coefficients. By increasing τ , these fine details vanish, and we obtain a rougher density estimator.

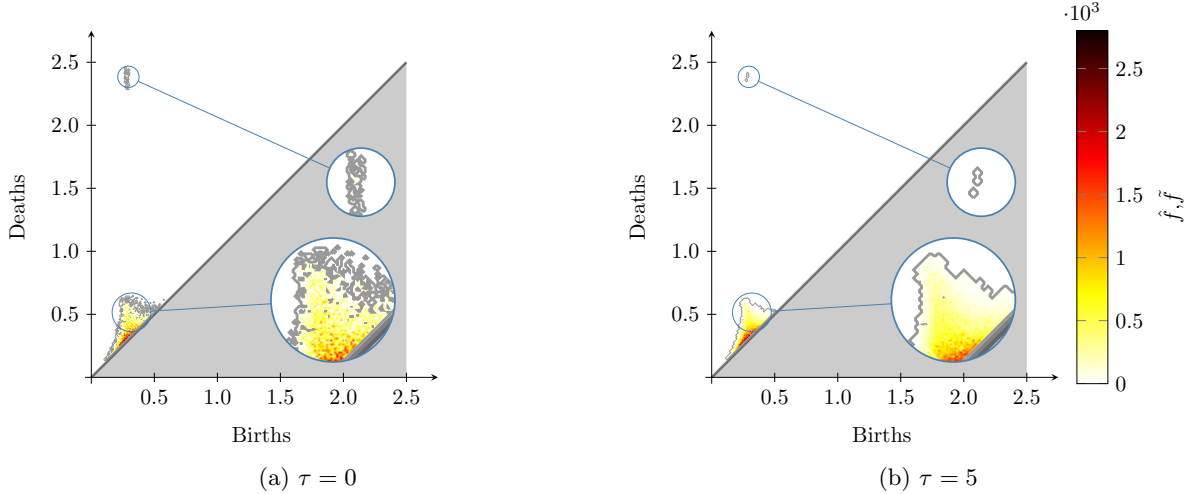


Figure 7: (a) The density of the Haar wavelet estimator, denoted \hat{f} , based on persistence diagrams of samples of a torus. (b) The density of a thresholding Haar wavelet estimator, denoted \tilde{f} . Here, we used grey contour lines to indicate the support of the density functions.

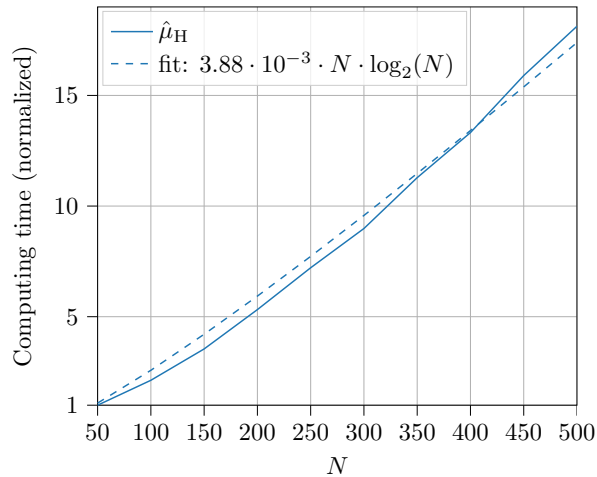


Figure 8: Computing time of Haar wavelet estimator for sample sizes $N \in \{50, \dots, 500\}$, where we normalized to the computing time corresponding to $N = 50$ (≈ 200 seconds on one CPU core).

We have analyzed the computational cost of the Haar wavelet estimator as a function of N , and Figure 8 shows that the runtime scales as $\mathcal{O}(N \log_2(N))$. This is consistent with what we would also expect in theory. Indeed, according to (12), the Haar wavelet estimator requires computing at most $\mathcal{O}(J + K) = \mathcal{O}(\log_2(N))$ wavelet coefficients, and computing a wavelet coefficient has complexity of order $\mathcal{O}(N)$. Thus, compared to the empirical mean $\bar{\mu}_N = \frac{1}{N} \sum_{i=1}^N \mu_i$, which clearly exhibits a computational complexity of $\mathcal{O}(N)$, the Haar wavelet estimator is computationally more expensive, but only by a logarithmic factor.

Double torus. We sample $n = 1000$ points uniformly at random from a double torus with inner and outer radii of 0.5 and 2, respectively, and add Gaussian noise with variance 0.5 to generate the point clouds $\{X_i\}_{i=1}^M$ and the persistence diagrams $\{\mu_i\}_{i=1}^M$, where $M = 10,000$. As in the previous example, the convergence rates of the Haar wavelet estimator (see Figure 9) coincide with the rates predicted by Theorem 9. In Figure 10, the convergence rates of the thresholding Haar wavelet estimator are shown, corresponding to the rates from Corollary 12.

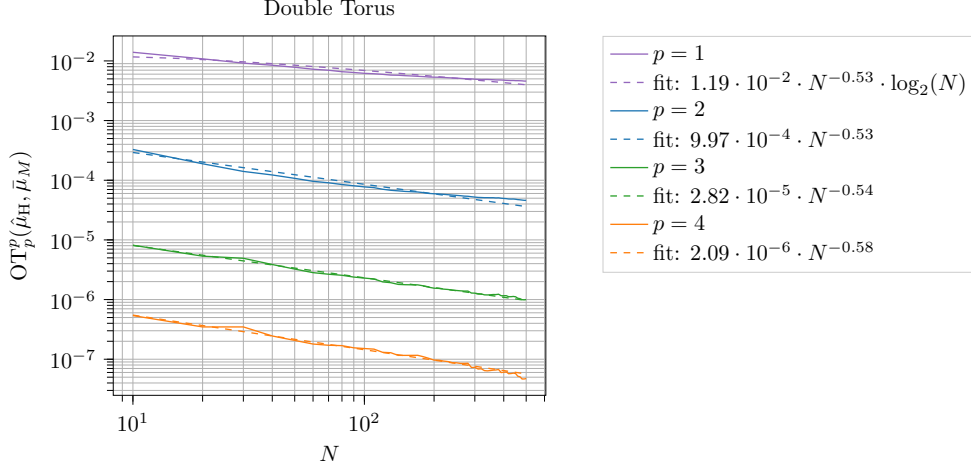


Figure 9: Convergence rates of the Haar wavelet estimator $\hat{\mu}_H$, averaged over 10 iterations, for different sample sizes N ranging from 10 to 500.

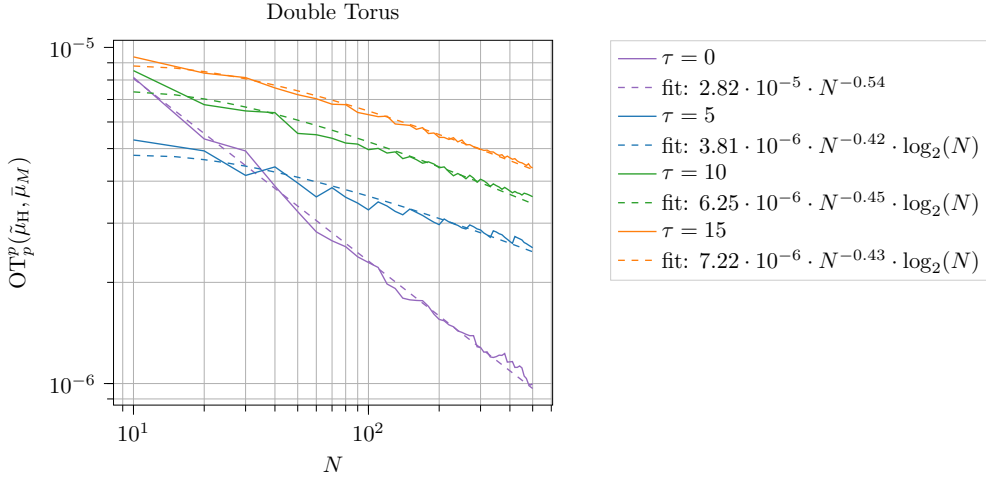


Figure 10: Convergence rates of the thresholding Haar wavelet estimator $\tilde{\mu}_H$, averaged over 10 iterations, where $N \in \{10, \dots, 500\}$ and $p = 3$.

Clustered process. Consider the following clustered process consisting of $n = 1000$ points. We first select uniformly at random $n_c = 4$ points from the square $[0, 1]^2$, denoted $\{c_i\}_{i=1}^{n_c}$, which serve as the clusters' centers. For each center c_i , $i \in \{1, \dots, n_c\}$, we generate $n/n_c = 250$ points by sampling from a Gaussian distribution with mean c_i and variance 0.1. Following this procedure, we create the point clouds $\{X_i\}_{i=1}^M$ and compute the corresponding persistence diagrams $\{\mu_i\}_{i=1}^M$, $M = 10,000$. Also in this example of a multimodal distribution, the convergence rates of the Haar wavelet estimator and the thresholding Haar wavelet estimator, provided respectively in [Figures 11](#) and [12](#), verify the results from [Theorem 9](#) and [Corollary 12](#).

4.2 An Application: Classification of a Dynamical System

We now demonstrate the utility of our proposed wavelet-based estimators by applying it to a core task in machine learning, namely, classification. We consider a discrete-time dynamical system previously studied topologically by (Conti *et al.*, 2022). The dynamical system models fluid flow as a linked twisted map and Poincaré section, in particular, which is the discretization of a continuous dynamical system given by following the location path of a particle at discrete time intervals. This linked twisted map is given by the

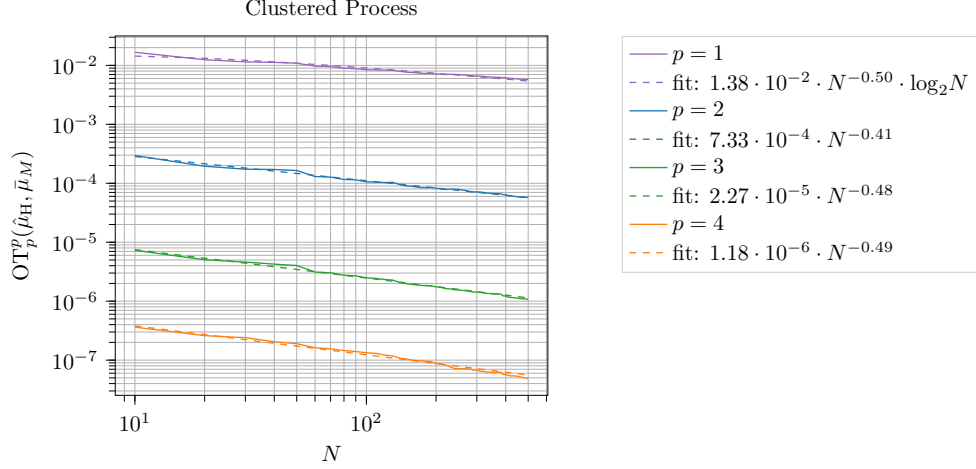


Figure 11: Convergence rates of the Haar wavelet estimator $\hat{\mu}_H$, averaged over 10 iterations, for $N \in \{10, \dots, 500\}$.

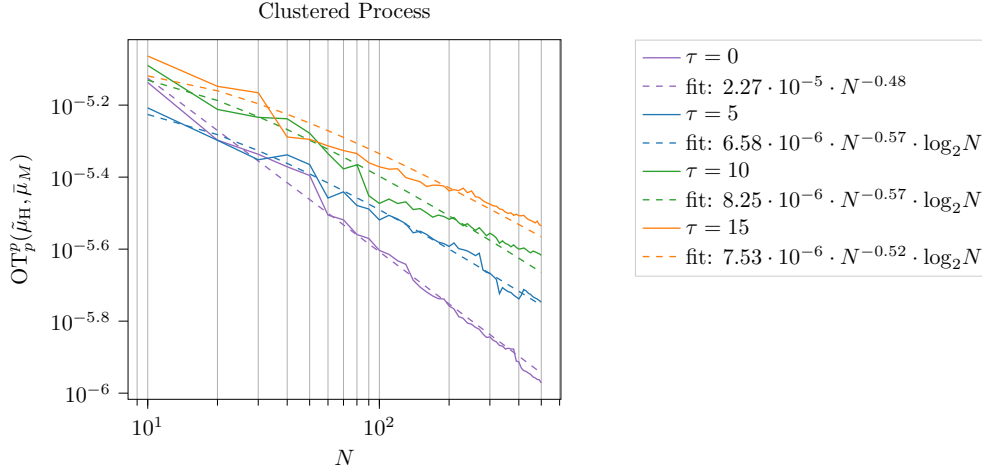


Figure 12: Convergence rates of the thresholding Haar wavelet estimator $\tilde{\mu}_H$, averaged over 10 iterations, for $N \in \{10, \dots, 500\}$, where $p = 3$.

following system of equations:

$$\begin{aligned} x_{k+1} &= (x_k + ry_k(1 - y_k)) \bmod 1, \\ y_{k+1} &= (y_k + rx_{k+1}(1 - x_{k+1})) \bmod 1, \end{aligned} \tag{45}$$

where the time index $k \in \mathbb{N}_0$, the initial conditions $(x_0, y_0) \in (0, 1)^2$ and $r > 0$. The orbits of this dynamical system, $\{(x_k, y_k) : k \in \mathbb{N}_0\}$, are used to model fluid flow. As shown by Conti *et al.* (2022), the shape of the orbit depends on the parameter r but not on the initial condition $(x_0, y_0) \in (0, 1)^2$ in general; see Figure 13. A machine learning task relevant to the study of such dynamical systems is to classify the value of the parameter r into the classes, based on the observed orbit $\{(x_k, y_k) : k \in \mathbb{N}_0\}$. We take the classes to be specified by five labels $\mathcal{R} := \{2, 3.5, 4, 4.1, 4.3\}$ as in (Conti *et al.*, 2022). To address this problem, we construct a dataset as follows.

For each class (label) $r \in \mathcal{R}$, $N = 100$ orbits $\{X_i^r\}_{i=1}^N$ of the form $\{(x_k, y_k) : 0 \leq k \leq n-1\}$, each consisting of $n = 1000$ points, are generated. From the orbits $\{X_i^r\}_{i=1}^N$, which can be viewed as point clouds in $[0, 1]^2$, the persistence diagrams $\{\mu_i^r\}_{i=1}^N$ are computed. Based on the persistence diagrams $\{\mu_i^r\}_{i=1}^N$, we compute the normalized Haar density estimator $\hat{\mu}_H^r$, for each class $r \in \mathcal{R}$. To successfully perform classification, it

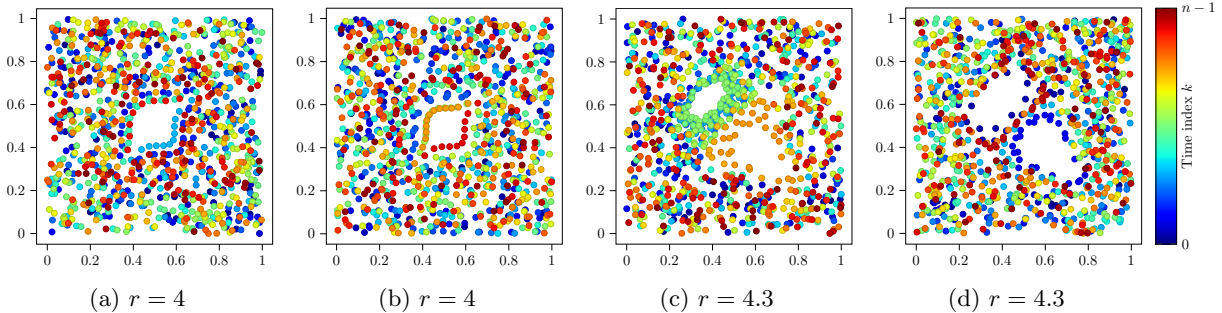


Figure 13: Examples of orbits $\{(x_k, y_k) : 0 \leq k \leq n-1\}$ of the dynamical system (45), consisting of $n = 1000$ points in $[0, 1]^2$. The orbits in (a) and (b) correspond to the same parameter, $r = 4$, but they have different initial conditions, namely, $(0.2, 0.1)$ and $(0.4, 0.9)$, respectively. The initial conditions in (c) and (d) are also $(0.2, 0.1)$ and $(0.4, 0.9)$, respectively.

essential that the estimated densities are sufficiently distinguishable, i.e., that $\hat{\mu}_H^r$ and $\hat{\mu}_H^{r'}$ are dissimilar for all distinct $r, r' \in \mathcal{R}$. Since these probability measures admit Lebesgue densities, we can quantify their (dis)similarity using the Hellinger distance, which is a metric between probability measures.

Definition 13 (Hellinger distance). Let ν_1 and ν_2 be two probability measures on Ω with Lebesgue densities g_1 and g_2 , respectively. The Hellinger distance between ν_1 and ν_2 is defined as $H(\nu_1, \nu_2) := \sqrt{H^2(\nu_1, \nu_2)}$, where

$$H^2(\nu_1, \nu_2) := \frac{1}{2} \int_{\Omega} \left(\sqrt{g_1(x)} - \sqrt{g_2(x)} \right)^2 dx.$$

The Hellinger distance $H(\nu_1, \nu_2)$ between two probability measures ν_1 and ν_2 admitting a Lebesgue density is symmetric, nonnegative, and it is zero if and only if $\nu_1 = \nu_2$. Moreover, an application of the Cauchy–Schwarz inequality shows that $0 \leq H(\nu_1, \nu_2) \leq 1$.

Computing the pairwise distances $H(\hat{\mu}_H^r, \hat{\mu}_H^{r'})$, $r, r' \in \mathcal{R}$, results in the 5×5 dissimilarity matrix presented in Figure 14(a). A value of 1 indicates complete dissimilarity between $\hat{\mu}_H^r$ and $\hat{\mu}_H^{r'}$, whereas 0 implies equality. Performing the same computations with the thresholding Haar wavelet estimator $\tilde{\mu}_H^r$ yields the results shown in Figure 14(b). Note that $H(\tilde{\mu}_H^r, \tilde{\mu}_H^{r'})$ is systematically smaller than $H(\hat{\mu}_H^r, \hat{\mu}_H^{r'})$, for all distinct $r, r' \in \mathcal{R}$, which results from the loss of accuracy when enforcing sparsity through thresholding. Nevertheless, we obtain that both $H(\hat{\mu}_H^r, \hat{\mu}_H^{r'})$ and $H(\tilde{\mu}_H^r, \tilde{\mu}_H^{r'})$ are close to 1 for all distinct $r, r' \in \mathcal{R}$. Thus, we can conclude that both the Haar wavelet estimator and the thresholding Haar wavelet estimator capture the topological differences in the trajectories generated by the different values of r and can be used to discriminate them.

Considering the case where only $N = 10$ orbits (and hence persistence diagrams) can be accessed, we infer from Figures 14(c) and 14(d) that these results still hold, showing that the classification performance of Haar wavelet-based estimators is robust to a decrease in sample size N .

Software and Data Availability

The Python code to implement all numerical experiments presented in this paper is publicly available and located on the Persistence Wavelets GitHub repository at

<https://github.com/konstantin-haberle/PersistenceWavelets>.

5 Discussion

In this work, we studied the distributional behavior of persistence diagrams in terms of the expected persistence diagram. We used the flexibility and accuracy of wavelets to nonparametrically estimate the density function describing the distribution. Specifically, we have shown that the Haar wavelet estimator $\hat{\mu}_H$ is a minimax estimator for the expected persistence diagram. In contrast to the empirical mean, which is a

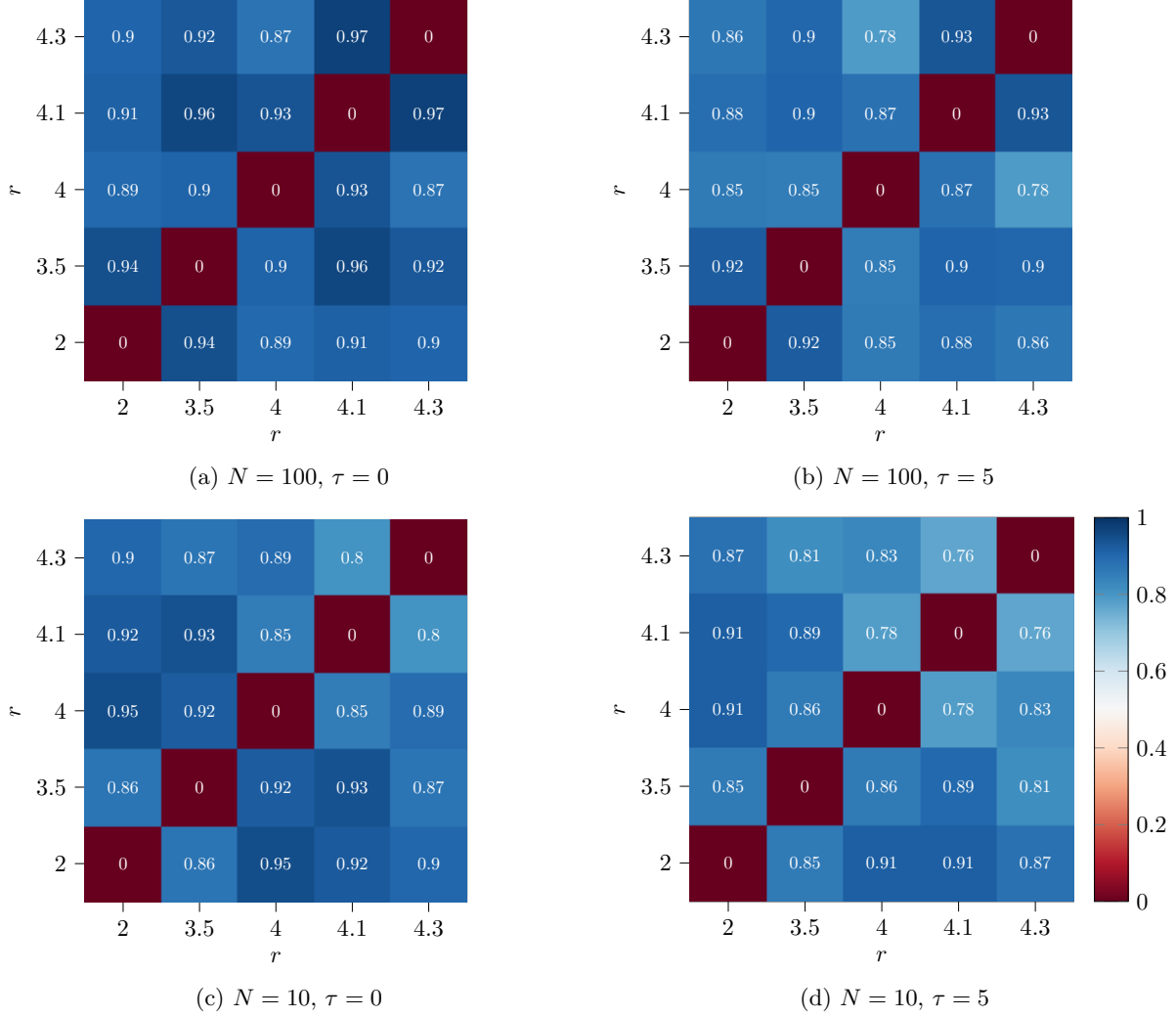


Figure 14: Pairwise Hellinger distances between the Haar wavelet estimators $\{\hat{\mu}_H^r\}_{r \in \mathcal{R}}$ for (a) $N = 100$ and (c) $N = 10$ as well as between the thresholding Haar wavelet estimators $\{\tilde{\mu}_H^r\}_{r \in \mathcal{R}}$ for (b) $N = 100$ and (d) $N = 10$. Values close to 1 (blue) indicate dissimilarity, while a value of 0 (red) represents equality.

discrete measure whose support is typically very large, $\hat{\mu}_H$ has a Lebesgue density. We also considered a Haar wavelet estimator which employs hard thresholding of the expansion coefficients, showing that it also achieves near-optimal convergence rates. This estimator, by retaining only the coefficients above a given threshold, offers a sparse representation of the expected persistence diagram. We verified the theoretical results by numerical experiments on two prototypical datasets in TDA, the torus and the double torus, as well as on a clustered process. These numerical results support our findings that Haar wavelets can provide an efficient and accurate process. The theoretical convergence rates are already apparent for modest sample sizes ($N \sim 100$), moreover, for the same sample size regime, a rather high degree of accuracy is achieved ($OT_p < 10^{-5}$ for $p > 1$ and $OT_p \sim 10^{-2}$ for $p = 1$). The computational complexity evaluating the Haar wavelet-based density estimator at a point in Ω scales as $\mathcal{O}(N \log_2(N))$. We characterized the effect of sparsity induced by hard thresholding, both at the level of the estimated density and its accuracy, showing that the OT_p magnitude stays comparable to that of Haar for a large set of thresholds and that there is a reduction in the occurrence of finely detailed features in the estimated density. Finally, we demonstrated the practical utility of the Haar wavelet density estimator by applying it to a classification task for dynamical trajectories. Our results illustrated that the proposed Haar

wavelet estimation techniques can effectively distinguish between classes of trajectories.

The application of tools from uncertainty quantification in TDA has a number of advantages. Density function estimation enables extrapolation to regions at low sampling as well as the reconstruction of structural features of the distribution of random persistence diagrams, such as gaps, which can lead to more robust insights into the underlying data topology. Due to their localized nature, wavelet transforms are particularly well-suited to capture the local features of the approximated signal. Hard thresholding of wavelet coefficients provides meaningful and sparse representation of the inputs that has been exploited for various applications, such as image compression and denoising (Krommweh, 2010; Fryzlewicz & Timmermans, 2016). This sparsity property may be exploited for various data reduction tasks when persistence diagrams consist of numerous points, and to facilitate feature extraction, which can be then leveraged for additional inference tasks, such as prediction and classification.

In general, wavelet transforms provide a multiresolution representation that is especially useful for signal decomposition and processing (Mallat, 1989). Thanks to their multiresolution representational properties, cascades of filters implementing wavelet transforms have been incorporated in convolutional neural networks, showing advantages in several settings (Bruna & Mallat, 2013; Pedersen *et al.*, 2022), and have been proposed as a mathematical framework to analyze deep convolutional architectures (Mallat, 2016). Multiresolution representations of the distribution of persistence diagrams are a promising perspective for further studies for their potential to gain a better understanding of the topology of complex datasets by enabling multiscale separation and the discovery of scale invariant features. These advantages may be incorporated in the advancement and development of machine learning algorithms for persistence diagrams.

Finally, the Haar basis is the simplest wavelet basis, but other bases, such as Symmlet wavelets, are often more suitable to approximate smooth functions. In particular, choosing an appropriate wavelet basis can lead to a sparser representation thanks to the regularity of the function to be estimated. Also the investigation on convergence could be extended to studying different wavelet transforms, such as Symmlet and Daubechies wavelets and Coiflets (Härdle *et al.*, 2012; Daubechies, 1992). These studies, however, would require alternative proof techniques since the construction employed here does not immediately extend to other types of wavelets. The majority of wavelet-based density estimation approaches rely on the empirical estimate of the wavelet series coefficients, as we did in this work, but it is also possible to take into account cases where the basis coefficients are learned via parametric estimators such as maximum likelihood (see, e.g., (Peter & Rangarajan, 2008)).

Acknowledgments

We wish to thank Mauricio Barahona, Yueqi Cao, Adi Ditzkowski, Théo Lacombe, and Primož Škraba for helpful discussions. We also would like to thank two anonymous referees for their helpful comments and suggestions which improved our work.

We wish to acknowledge the Information and Communication Technologies resources at Imperial College London for their computing resources which were used to implement the experiments in this paper.

References

- ABRAMOVICH, FELIX, BAILEY, TREVOR C, & SAPATINAS, THEOFANIS. 2000. Wavelet analysis and its statistical applications. *Journal of the Royal Statistical Society: Series D (The Statistician)*, **49**(1), 1–29.
- ADAMS, HENRY, EMERSON, TEGAN, KIRBY, MICHAEL, NEVILLE, RACHEL, PETERSON, CHRIS, SHIPMAN, PATRICK, CHEPUSHSTANOVA, SOFYA, HANSON, ERIC, MOTTA, FRANCIS, & ZIEGELMEIER, LORI. 2017. Persistence images: A stable vector representation of persistent homology. *Journal of Machine Learning Research*, **18**.
- BRUNA, JOAN, & MALLAT, STÉPHANE. 2013. Invariant scattering convolution networks. *IEEE Transactions on Pattern Analysis and Machine Intelligence*, **35**(8), 1872–1886.
- BUBENIK, PETER. 2015. Statistical topological data analysis using persistence landscapes. *J. Mach. Learn. Res.*, **16**(1), 77–102.

- BUBENIK, PETER, & WAGNER, ALEXANDER. 2020. Embeddings of persistence diagrams into Hilbert spaces. *Journal of Applied and Computational Topology*, **4**(3), 339–351.
- CHAZAL, FRÉDÉRIC, & DIVOL, VINCENT. 2019. The density of expected persistence diagrams and its kernel based estimation. *Journal of Computational Geometry*, **10**(2), 127–153.
- COHEN, ALBERT. 2003. *Numerical analysis of wavelet methods*. Elsevier.
- CONTI, FRANCESCO, MORONI, DAVIDE, & PASCALI, MARIA ANTONIETTA. 2022. A topological machine learning pipeline for classification. *Mathematics*, **10**(17), 3086.
- CRAWFORD, LORIN, MONOD, ANTHEA, CHEN, ANDREW X., MUKHERJEE, SAYAN, & RABADÁN, RAÚL. 2020. Predicting Clinical Outcomes in Glioblastoma: An Application of Topological and Functional Data Analysis. *Journal of the American Statistical Association*, **115**(531), 1139–1150.
- DAUBECHIES, INGRID. 1992. *Ten lectures on wavelets*. SIAM.
- DIVOL, VINCENT, & LACOMBE, THÉO. 2021a. Estimation and quantization of expected persistence diagrams. *Pages 2760–2770 of: International Conference on Machine Learning*. PMLR.
- DIVOL, VINCENT, & LACOMBE, THÉO. 2021b. Understanding the topology and the geometry of the space of persistence diagrams via optimal partial transport. *Journal of Applied and Computational Topology*, **5**(1), 1–53.
- DONOHO, DAVID L., JOHNSTONE, IAIN M., KERKYACHARIAN, GÉRARD, & PICARD, DOMINIQUE. 1996. Density estimation by wavelet thresholding. *The Annals of Statistics*, **24**(2), 508–539.
- FLAMARY, RÉMI, COURTY, NICOLAS, GRAMFORT, ALEXANDRE, ALAYA, MOKHTAR Z., BOISBUNON, AURÉLIE, CHAMBON, STANISLAS, CHAPEL, LAETITIA, CORENFLOS, ADRIEN, FATRAS, KILIAN, FOURNIER, NEMO, GAUTHERON, LÉO, GAYRAUD, NATHALIE T.H., JANATI, HICHAM, RAKOTOMAMONJY, ALAIN, REDKO, IEVGEN, ROLET, ANTOINE, SCHUTZ, ANTONY, SEGUY, VIVIEN, SUTHERLAND, DANICA J., TAVENARD, ROMAIN, TONG, ALEXANDER, & VAYER, TITOUAN. 2021. POT: Python Optimal Transport. *Journal of Machine Learning Research*, **22**(78), 1–8.
- FOURNIER, NICOLAS, & GUILLIN, ARNAUD. 2015. On the rate of convergence in Wasserstein distance of the empirical measure. *Probability Theory and Related Fields*, **162**(3-4), 707–738.
- FRYZLEWICZ, PIOTR, & TIMMERMANS, CATHERINE. 2016. SHAH: SHape-Adaptive Haar wavelets for image processing. *Journal of Computational and Graphical Statistics*, **25**(3), 879–898.
- HÄRDLE, WOLFGANG, KERKYACHARIAN, GERARD, PICARD, DOMINIQUE, & TSYBAKOV, ALEXANDER. 2012. *Wavelets, approximation, and statistical applications*. Vol. 129. Springer Science & Business Media.
- KANG, IN, HUDSON, IRENE, RUDGE, ANDREW, & CHASE, J GEOFFREY. 2013. Density estimation and wavelet thresholding via Bayesian methods: A wavelet probability band and related metrics approach to assess agitation and sedation in ICU patients. *Discrete Wavelet Transforms: A Compendium of New Approaches and Recent Applications*. 1st ed. Rijeka: IntechOpen, 127–162.
- KROMMWEH, JENS. 2010. Tetrolet transform: A new adaptive Haar wavelet algorithm for sparse image representation. *Journal of Visual Communication and Image Representation*, **21**(4), 364–374.
- LI, CHUNYUAN, OVSJANIKOV, MAK, & CHAZAL, FRÉDÉRIC. 2014. Persistence-Based Structural Recognition. *Pages 2003–2010 of: 2014 IEEE Conference on Computer Vision and Pattern Recognition*.
- MALLAT, STÉPHANE. 2016. Understanding deep convolutional networks. *Philosophical Transactions of the Royal Society A: Mathematical, Physical and Engineering Sciences*, **374**(2065), 20150203.
- MALLAT, STEPHANE G. 1989. A theory for multiresolution signal decomposition: the wavelet representation. *IEEE Transactions on Pattern Analysis and Machine Intelligence*, **11**(7), 674–693.

- MILEYKO, YURIY, MUKHERJEE, SAYAN, & HARER, JOHN. 2011. Probability measures on the space of persistence diagrams. *Inverse Problems*, **27**(12), 124007.
- MONOD, ANTHEA, KALIŠNIK, SARA, PATIÑO GALINDO, JUAN ÁNGEL, & CRAWFORD, LORIN. 2019. Tropical Sufficient Statistics for Persistent Homology. *SIAM Journal on Applied Algebra and Geometry*, **3**(2), 337–371.
- PEDERSEN, CHRISTIAN, EICKENBERG, MICHAEL, & HO, SHIRLEY. 2022. Learnable wavelet neural networks for cosmological inference. *In: ICML 2022 Workshop on Machine Learning for Astrophysics*.
- PEREA, JOSE A, & HARER, JOHN. 2015. Sliding windows and persistence: An application of topological methods to signal analysis. *Foundations of Computational Mathematics*, **15**(3), 799–838.
- PETER, ADRIAN M, & RANGARAJAN, ANAND. 2008. Maximum likelihood wavelet density estimation with applications to image and shape matching. *IEEE Transactions on Image Processing*, **17**(4), 458–468.
- REININGHAUS, JAN, HUBER, STEFAN, BAUER, ULRICH, & KWITT, ROLAND. 2015. A stable multi-scale kernel for topological machine learning. *Pages 4741–4748 of: Proceedings of the IEEE conference on computer vision and pattern recognition*.
- TAUZIN, GUILLAUME, LUPO, UMBERTO, TUNSTALL, LEWIS, PÉREZ, JULIAN BURELLA, CAORSI, MATTEO, MEDINA-MARDONES, ANIBAL, DASSATTI, ALBERTO, & HESS, KATHRYN. 2020. *giotto-tda: A Topological Data Analysis Toolkit for Machine Learning and Data Exploration*.
- THE GUDHI PROJECT. 2015. *GUDHI User and Reference Manual*. GUDHI Editorial Board.
- TURNER, KATHARINE, MILEYKO, YURIY, MUKHERJEE, SAYAN, & HARER, JOHN. 2014. Fréchet means for distributions of persistence diagrams. *Discrete & Computational Geometry*, **52**(1), 44–70.
- WEED, JONATHAN, & BACH, FRANCIS. 2019. Sharp asymptotic and finite-sample rates of convergence of empirical measures in Wasserstein distance. *Bernoulli*, **25**(4A), 2620–2648.
- ZHAO, QIBIN, & ZHANG, LIQING. 2005. ECG feature extraction and classification using wavelet transform and support vector machines. *Pages 1089–1092 of: 2005 International Conference on Neural Networks and Brain*, vol. 2. IEEE.
- ZOMORODIAN, AFRA, & CARLSSON, GUNNAR. 2005. Computing Persistent Homology. *Discrete & Computational Geometry*, **33**(2), 249–274.